ATLAS CONF Note

ATLAS-CONF-2020-002

20th February 2020

Search for new phenomena in final states with large jet multiplicities and missing transverse momentum using $\sqrt{s}$ = 13 TeV proton–proton collisions recorded by ATLAS in Run 2 of the LHC

The ATLAS Collaboration

Results of a search for new particles decaying to eight or more jets and moderate missing transverse momentum are presented. The analysis uses 139 fb^{-1} of proton–proton collision data at $\sqrt{s}$ = 13 TeV collected by the ATLAS experiment at the Large Hadron Collider between 2015 and 2018. The selection rejects events containing isolated electrons or muons, and makes requirements according to the number of b-tagged jets and the scalar sum of masses of large-radius jets. The search extends previous analyses both in using a larger dataset and by employing improved jet and missing transverse momentum reconstruction methods which more cleanly separate signal from background processes. No evidence for physics beyond the Standard Model is found. The results are interpreted in the context of supersymmetry-inspired simplified models, significantly extending the limits on the gluino mass in those models. In particular, limits on the gluino mass are set at 2 TeV when the lightest neutralino is nearly massless in a model assuming a two-step cascade decay via the lightest chargino and second-lightest neutralino.

ATLAS-CONF-2020-002
20 February 2020

1 Introduction

The Large Hadron Collider [1] (LHC) has produced a large dataset of proton–proton (pp) collisions at a centre-of-mass energy of 13 TeV enabling searches for new heavy particles predicted by theories such as supersymmetry (SUSY) [2–7]. Evidence for SUSY models may be sought through searches for the production of these heavy particles (such as gluinos) decaying, often via extended cascades, to lighter ones. If the lightest of these interacts only weakly and is stable then it can be an ideal dark matter candidate.

In R-parity-conserving (RPC) [8] SUSY models, the presence of a stable lightest supersymmetric particle (LSP) often leads to final states with significant missing transverse momentum ($E_{\mathrm{T}}^{\mathrm{miss}}$), often accompanied by a large number of jets. Large jet multiplicities would also occur in events in which gluinos decay via R-parity-violating (RPV) [9] couplings on short ($\lesssim$ns) timescales. In this case the LSPs decay within the detector volume, so that the only invisible particles produced are neutrinos coming from SUSY particle decays, hence the $E_{\mathrm{T}}^{\mathrm{miss}}$ per event is generally smaller. A similar signature may also arise from any model in which cascade decays lead to the production of many jets, together with $E_{\mathrm{T}}^{\mathrm{miss}}$ either from dark matter particles or neutrinos.

This note reports the results of an analysis of 139 fb^{-1} of pp collision data recorded at $\sqrt{s}$ = 13 TeV by the ATLAS experiment [10] throughout the entire Run-2 period of the LHC (2015–2018). It explores events with significant $E_{\mathrm{T}}^{\mathrm{miss}}$ and at least eight jets with a large transverse momentum (p_{T}). Selected events are further classified based on the presence of jets containing b-hadrons (b-jets) or on the sum of the masses of large-radius jets. The b-jet selection improves sensitivity to beyond-the-Standard-Model (BSM) signals with enhanced heavy-flavour decays. Given the unusually high jet multiplicities of the selected events, large jet masses can originate both from the capture of decay products from boosted heavy particles, including top quarks, and from accidental combinations [11]. The major backgrounds to this search are multijet production from QCD processes, top quark pair production ($t\bar{t}$) and W boson production in association with jets (W+jets).

Previous searches by ATLAS in similar final states were carried out on smaller LHC datasets recorded at $\sqrt{s}$ = 7 and 8 TeV from 2011–2012 [12–14]. In addition, two searches were performed at $\sqrt{s}$ = 13 TeV, one analysing the 2015 dataset [15] and one combining it with 2016 data [16] to achieve a total integrated luminosity of 36 fb^{-1}. The current analysis extends those previous studies by including the complete Run-2 LHC dataset, by using an optimised selection tailored to the increased integrated luminosity, and also by incorporating several improved analysis methods which further increase sensitivity. One such development is the use of the particle-flow jet and $E_{\mathrm{T}}^{\mathrm{miss}}$ reconstruction algorithms recently developed for the ATLAS experiment [17]. These algorithms combine measurements of inner tracker and calorimeter deposits to improve the accuracy of the charged-hadron measurement, leading to improvements in the jet and $E_{\mathrm{T}}^{\mathrm{miss}}$ resolution and stability against additional pp interactions in the same LHC bunch crossing. The analysis also employs an improved $E_{\mathrm{T}}^{\mathrm{miss}}$ significance calculation [18], which accounts for the resolution of the reconstructed objects individually. This new definition increases the separation between events in which the $E_{\mathrm{T}}^{\mathrm{miss}}$ originates from weakly interacting particles and those in which $E_{\mathrm{T}}^{\mathrm{miss}}$ is only due to detector resolution effects. The combination of the larger dataset and the developments in the analysis methodology leads to a significantly increased mass range over which the analysis has sensitivity.

2 ATLAS detector

The ATLAS detector [10] is a multipurpose particle detector with a nearly 4π coverage in solid angle.[1] It consists of an inner tracking detector (ID) surrounded by a thin superconducting solenoid providing a 2 T axial magnetic field, electromagnetic (EM) and hadronic calorimeters, and a muon spectrometer. The inner tracking detector covers the pseudorapidity range $|\eta| < 2.5$. It consists of silicon pixel, silicon microstrip, and transition radiation tracking detectors. A new inner pixel layer, the insertable B-layer [19, 20], was added at a mean radius of 3.3 cm before the start of the 2015 data-taking period, improving the identification of b-jets. Lead/liquid-argon (LAr) sampling calorimeters provide EM energy measurements with high granularity. A steel/scintillator-tile hadron calorimeter covers the central pseudorapidity range ($|\eta| < 1.7$). The endcap and forward regions are instrumented with LAr calorimeters for EM and hadronic energy measurements up to $|\eta| = 4.9$. The muon spectrometer surrounds the calorimeters and is based on three large air-core toroidal superconducting magnets with eight coils each. The field integral of the toroids ranges between 2.0 and 6.0 Tm across most of the detector. The muon spectrometer includes a system of precision tracking chambers and fast detectors for triggering. A two-level trigger system [21] is used to select events. The first-level trigger is implemented in hardware and uses a subset of the detector information to keep the accepted rate below 100 kHz. This is followed by a software-based trigger that reduces the accepted event rate to 1 kHz on average depending on the data-taking conditions.

3 Datasets

3.1 Data

The events considered in this note correspond to 139 fb^{-1} of pp LHC collision data collected between 2015 and 2018 by the ATLAS detector, at a centre-of-mass energy of 13 TeV and with a 25 ns proton bunch crossing interval. In 2015–2016 the average number of interactions per bunch crossing (pile-up) was $\langle\mu\rangle = 20$, increasing to $\langle\mu\rangle = 38$ in 2017 and $\langle\mu\rangle = 37$ in 2018. The uncertainty in the combined 2015–2018 integrated luminosity is 1.7% [22], obtained using the LUCID-2 detector [23] for the primary luminosity measurements.

Events were recorded using a variety of trigger selections. During both 2015 and 2016, events were selected by a trigger requiring at least six jets with $E_{\mathrm{T}} > 45$ GeV and central pseudorapidity, $|\eta| < 2.4$. Further events were triggered in 2015 by requiring the presence of at least five jets with $E_{\mathrm{T}} > 70$ GeV and $|\eta| < 3.2$, and in 2016 with a trigger requiring at least five jets with $E_{\mathrm{T}} > 65$ GeV and $|\eta| < 2.4$. In both 2017 and 2018, events were selected by triggers requiring at least five jets with $E_{\mathrm{T}} > 70$ GeV and $|\eta| < 2.4$, or seven jets with $E_{\mathrm{T}} > 45$ GeV and $|\eta| < 2.4$. Additional triggers were also used in 2017 and for some periods in 2018, which required at least six jets with $E_{\mathrm{T}} > 45$ GeV and $|\eta| < 2.4$. Due to their large trigger rates, these selected only a fraction of events, approximately 15% of the two years' data; such triggers are denoted as 'prescaled' triggers. The trigger jet calibration was improved in 2017–2018, resulting in substantially better

[1] ATLAS uses a right-handed coordinate system with its origin at the nominal interaction point in the centre of the detector. The positive x-axis is defined by the direction from the interaction point to the centre of the LHC ring, with the positive y-axis pointing upwards, while the beam direction defines the z-axis. Cylindrical coordinates (r, ϕ) are used in the transverse plane, ϕ being the azimuthal angle around the z-axis. The pseudorapidity η is defined in terms of the polar angle θ by $\eta = -\ln\tan(\theta/2)$. The rapidity is defined as $y = 0.5\ln[(E + p_z)/(E - p_z)]$ where E denotes the energy and p_z is the component of the momentum along the beam direction. The angular distance ΔR is defined as $\sqrt{(\Delta y)^2 + (\Delta\phi)^2}$.

efficiency [24] after offline selection for the same trigger thresholds. The trigger selections are summarised later in Table 1 together with further event selections.

Data quality requirements are imposed to ensure that only events in which the entire ATLAS detector was functioning well are used [25]. These, for example, exclude events containing data corruption in the ID and calorimeters, excessive noise and spurious jets produced by non-collision backgrounds [26, 27].

3.2 Monte Carlo simulations

Simulated events produced with several Monte Carlo (MC) event generators are used to predict yields for subdominant background contributions from Standard Model (SM) processes and for possible signals.

All simulated events are overlaid with multiple pp collisions simulated with the soft QCD processes of Pythia 8.186 [28] using the A3 set of parameters (A3 tune) [29] and the NNPDF2.3 LO parton distribution functions (PDFs) [30]. The simulated events are required to pass the trigger selections, and are weighted such that the pile-up conditions match those of the data. The response of the detector to particles is modelled with an ATLAS detector simulation [31] based on Geant4 [32] (full simulation), or using fast simulation based on a parameterisation of the performance of the ATLAS electromagnetic and hadronic calorimeters [33] and on Geant4 elsewhere.

For the generation of $t\bar{t}$ and single top quarks via the Wt process and in the s-channel, matrix elements are calculated at next-to-leading-order (NLO) using the Powheg-Box v2 generator [34–39] with the NNPDF3.0 NLO PDF set [40] in the five-flavour scheme. Electroweak t-channel single-top-quark events are generated using Powheg-Box v2, using the four-flavour scheme for the NLO matrix element calculations together with the fixed four-flavour PDF set NNPDF3.04f NLO. The Diagram Removal (DR) scheme [41] is used to prevent Wt events from being counted as $t\bar{t}$ events beyond leading-order (LO). For these processes, the top quarks are decayed using MadSpin [42] preserving all spin correlations, while for all processes the parton shower, fragmentation, and the underlying event are simulated using Pythia 8.230 [43] with the NNPDF2.3 LO PDF set and the ATLAS A14 tune [44]. The top quark mass is set to 172.5 GeV. The h_{damp} parameter, which controls the p_{T} of the first additional emission beyond the Born configuration in Powheg, is set to 1.5 times the mass of the top quark. The main effect of this parameter is to regulate the high-p_{T} emission against which the $t\bar{t}$ system recoils. The EvtGen v1.6.0 program [45] is used to model properties of the b- and c-hadron decays for this process and all others not simulated with Sherpa [46] unless otherwise stated. Simulated $t\bar{t}$ events are normalised to the cross-section calculated to next-to-next-to-leading order (NNLO) in perturbative QCD, including soft-gluon resummation to next-to-next-to-leading-logarithm (NNLL) order [47]. The single-top-quark events for the Wt channel are normalised using its approximate NNLO prediction [48, 49], while the t- and s-channels are normalised using their NLO predictions [50, 51].

Events containing $t\bar{t}$ and additional heavy particles – comprising three or four top quarks, $t\bar{t}+W$, $t\bar{t}+Z$ and $t\bar{t}+WW$ production – are simulated at LO in the strong coupling constant α_{S}, using MadGraph5 [52] with up to two additional partons in the matrix element, interfaced to the Pythia 8 parton shower model. For the $t\bar{t}+WW$, three- and four-top-quark processes, MadGraph5_aMC@NLO v2.2.2 is used with Pythia 8.186, and for $t\bar{t}+W$ and $t\bar{t}+Z$, MadGraph5_aMC@NLO v2.3.3 is used with Pythia 8.210. The A14 set of Pythia 8 parameters is used, together with the NNPDF2.3 LO PDF set. EvtGen v1.2.0 is used to model properties of the b- and c-hadron decays. The predicted production cross-sections are calculated to NLO as described in Ref. [52]. The contribution from $t\bar{t}+H$ has been checked and found to be negligible.

Events containing W or Z bosons associated with jets are simulated using the Sherpa v2.2.1 generator. Matrix elements are calculated for up to two partons at NLO and four partons at LO using the Comix [53] and OpenLoops [54] matrix element generators and merged with the Sherpa parton shower [55] using the ME+PS@NLO prescription [56]. The NNPDF3.0 NNLO PDF set [40] is used in association with a tuning performed by the Sherpa authors.

Diboson processes with one hadronically decaying boson accompanied by one charged lepton and one neutrino, two charged leptons or two neutrinos are simulated using Sherpa v2.1.1. The calculations include one additional parton at NLO for $ZZ \to 2\ell + q\bar{q}$ and $ZZ \to 2\nu + q\bar{q}$ only, and up to three additional partons at LO using the Comix and OpenLoops matrix element generators and merged with the Sherpa parton shower using the ME+PS@NLO prescription. The NNPDF3.0 NNLO PDF set is used in conjunction with a dedicated parton shower tuning developed by the Sherpa authors. Diboson processes with four charged leptons, three charged leptons and one neutrino, or two charged leptons and two neutrinos, are found to be negligible.

Theoretical uncertainties are considered for all simulated samples. By far the most important process simulated in this analysis is $t\bar{t}$ production, and several samples produced with different configurations, as explained below, are compared to estimate the uncertainty in this background. Samples have been produced with the factorisation and renormalisation scales varied coherently up and down by a factor of two, and with parameters set to provide more/less radiation in the parton shower [57]. Additionally, to account for uncertainties from the parton shower modelling and generator choice, the nominal sample is compared to a sample generated with Powheg-Box interfaced to Herwig 7 [58] using the H7-UE tune [59] and the MMHT2014 LO PDF set [60], as well as samples generated with MadGraph5_aMC@NLO interfaced to Pythia 8. These alternative samples each use the NNPDF3.0 NLO PDF for the matrix element. The comparison with samples which vary the amount of additional radiation contributes the largest uncertainty in the $t\bar{t}$ signal region predictions. Similar alternative samples are used to assess the uncertainties on single-top-quark production, whereas uncertainties on other processes are handled via scale variations in the corresponding generator.

Full simulation is used for all background MC samples, ensuring an accurate representation of detector effects. Further details of samples can be found in Refs. [57, 61, 62].

A number of SUSY signal model samples are simulated using the ATLAS fast detector simulation [31] to allow the interpretation of the search results in terms of SUSY parameters. Substantial cross-sections are possible for production of gluinos. The resulting cascade decays result in a large multiplicity of jets, and may also exhibit an unusually high heavy-flavour content or atypically large jet masses.

The first type of SUSY signal simulated is a simplified model, in which gluinos are pair-produced and then decay through an off-shell squark via the cascade:

$$\begin{aligned} \tilde{g} &\to q + \bar{q}' + \tilde{\chi}_1^{\pm} \quad (q, q' \in \{u, d, s, c\}), \\ \tilde{\chi}_1^{\pm} &\to W^{\pm} + \tilde{\chi}_2^0, \\ \tilde{\chi}_2^0 &\to Z + \tilde{\chi}_1^0, \end{aligned}$$

where the quarks are only permitted to be from the first two generations. The parameters of the model are the masses of the gluino, $m_{\tilde{g}}$, and the lightest neutralino, $m_{\tilde{\chi}_1^0}$. The mass of the $\tilde{\chi}_1^{\pm}$ is constrained to be $(m_{\tilde{g}} + m_{\tilde{\chi}_1^0})/2$, and the mass of the $\tilde{\chi}_2^0$ is set to $(m_{\tilde{\chi}_1^{\pm}} + m_{\tilde{\chi}_1^0})/2$. A diagram of this "two-step" simplified model is shown in Figure 1(a).

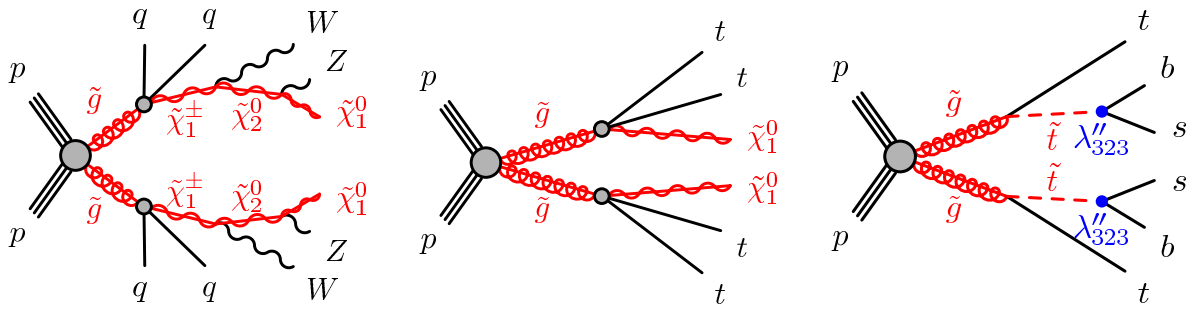

(a) Two-step decay (b) Off-shell top squarks (c) RPV

Figure 1: Pseudo-Feynman diagrams for the different signal models used in this search. λ''_{323} in (c) is one of the couplings of the third generation squark to quarks in the RPV model.

An additional signal model to which this analysis has significant sensitivity is gluino-mediated top squark ($\tilde{t}_1$) production, in which top-quark-rich final states are produced as shown in Figure 1(b). This model manifests itself as top quark production via either off-shell or on-shell top squarks. In the off-shell model, pair-production of gluinos is followed by their decay with a 100% branching ratio to $t\bar{t} + \tilde{\chi}_1^0$, through a virtual top squark. Naturalness arguments for SUSY favour light gluinos, top squarks, and Higgsinos, so motivate consideration of this final state.

Permitting non-zero RPV couplings allows consideration of another variety of gluino-mediated top squark production, wherein the last step of the decay proceeds via a baryon-number-violating interaction: $\tilde{t}_1 \rightarrow \bar{s} + \bar{b}$ (charge conjugates implied). Such RPV models may give rise to final states with missing transverse momentum, for example from leptonic decays of W bosons produced in top quark decays. The current analysis accepts final states with sufficiently low missing transverse momentum to be sensitive to these RPV scenarios. Figure 1(c) presents the RPV simplified model considered, for which the coupling strength induces prompt top squark decays.

The signal samples are generated using MadGraph5_aMC@NLO interfaced to Pythia 8 with the A14 tune for the modelling of the parton shower, hadronisation and underlying event. The versions of the generators used for the two-step and RPV simplified models are MadGraph5_aMC@NLO v2.6.2 with Pythia 8.212, and for the gluino-mediated top squark model MadGraph5_aMC@NLO v2.3.3 with Pythia 8.212. The matrix element calculation is performed at tree level and includes the emission of up to two additional partons. The PDF set used for the generation is NNPDF2.3 LO. The EvtGen v1.6.0 program is used to simulate properties of the b- and c-hadron decays. The matrix-element to parton-shower matching is done using the CKKW-L prescription [63], with a matching scale set to $m_{\tilde{g}}/4$.

Signal cross-sections are calculated to approximate NNLO in the strong coupling constant, adding the resummation of soft gluon emission at NNLL accuracy [64–71]. The nominal cross-section and the uncertainty are derived using the PDF4LHC15_mc PDF set, following the recommendations of Ref. [72].

4 Reconstruction and particle identification

Primary vertices are reconstructed using at least two charged-particle tracks with $p_{\mathrm{T}} > 500$ MeV measured by the ID [73]. The primary vertex with the largest sum of squared track transverse momenta ($\sum p_{\mathrm{T}}^2$) is designated as the hard scatter vertex.

Jets are reconstructed using the anti-k_t [74] jet algorithm with radius parameter $R = 0.4$. It uses as inputs particle-flow objects, which are charged-particle tracks matched to the hard scatter vertex with the requirement $|z_0 \sin\theta| < 2.0$ mm, where z_0 is the longitudinal impact parameter, and calorimeter energy clusters surviving an energy subtraction algorithm that removes the calorimeter deposits of good-quality tracks from any vertex [17]. To eliminate jets containing a large energy contribution from pile-up, jets are tested for compatibility with the hard scatter vertex with the jet vertex tagger (JVT) discriminant, utilising information from the ID tracks associated with the jet [75]. Any jets with 20 GeV$< p_{\mathrm{T}} < 120$ GeV and $|\eta| < 2.4$ for which JVT < 0.5 are considered to originate from pile-up and are therefore rejected from the analysis. After the selection above is applied, only jets with $p_{\mathrm{T}} > 20$ GeV and $|\eta| < 2.8$ are considered in this analysis, with the exception of the $E_{\mathrm{T}}^{\mathrm{miss}}$ calculation, for which jets in the range $2.8 \leq |\eta| \leq 4.5$ are also used. Hadronically decaying τ-leptons are not discriminated from other hadronic jets.

Jets with radius parameter $R = 0.4$, with $p_{\mathrm{T}} > 20$ GeV and $|\eta| < 2.0$ are reclustered to form large-radius jets using the anti-k_t algorithm with radius parameter $R = 1.0$ [76]. The input jets are required to pass an overlap removal procedure accounting for ambiguities between jets and leptons, as discussed below. Large-radius jets are retained for analysis if they have $p_{\mathrm{T}} > 100$ GeV and $|\eta| < 1.5$.

Jets containing b-hadrons and which are within the ID acceptance ($|\eta| < 2.5$) are identified as b-tagged jets using a multivariate algorithm that exploits the impact parameters of the charged-particle tracks, the presence of secondary vertices, and the reconstructed flight paths of b- and c-hadrons inside the jet [77]. The output of the algorithm is a single discriminant value which signifies the likelihood of a jet containing b-hadrons. This analysis considers jets to be b-tagged if the discriminant exceeds a threshold that results in an average identification efficiency of 70% for jets containing b-hadrons in simulated $t\bar{t}$ events [78]. In the same event sample, a rejection factor of approximately 300 is reached for jets initiated by light quarks and gluons and 8.9 for jets initiated by charm quarks.

Electron candidates are reconstructed from energy deposits in the EM calorimeter that are matched to charged-particle tracks in the ID [79]. "Baseline electrons" are required to satisfy $p_{\mathrm{T}} > 7$ GeV and $|\eta| < 2.47$. They are identified using the "loose" operating point provided by a likelihood-based algorithm [79]. Electrons with $p_{\mathrm{T}} > 20$ GeV are defined as signal electrons by requiring a "tight" likelihood selection including impact parameter restrictions and the "GradientLoose" isolation requirement [80] in addition to the preselection. To achieve additional rejection of background electrons from non-prompt sources, signal electron tracks must be matched to the hard scatter vertex with a longitudinal impact parameter $|z_0 \sin\theta| < 0.5$ mm and a transverse impact parameter significance $|d_0|/\sigma(d_0) < 5$. Signal electrons are used in leptonic control regions, as described in Section 6.2. The electron reconstruction and identification efficiency in simulated samples are corrected by factors determined by data-MC comparison using a given final state [80].

Photon candidates are identified using "tight" criteria defined by lateral shower shapes in the first and second layers of the EM calorimeter, as well as the degree of hadronic shower leakage [79]. Acceptance requirements of $p_{\mathrm{T}} > 40$ GeV and $|\eta| < 2.37$ are applied. Additionally, photons falling in the region $1.37 < |\eta| < 1.52$ are removed, to avoid a poorly instrumented region of the calorimeter.

Muon candidates are reconstructed from matching tracks in the ID and muon spectrometer, refined through a global fit which uses the hits from both subdetectors [81]. "Baseline muons" must have $p_{\mathrm{T}} > 6$ GeV and $|\eta| < 2.7$, and satisfy the "medium" identification criteria. Similarly to electrons, the longitudinal impact parameter z_0 relative to the hard scatter vertex is required to satisfy $|z_0 \sin\theta| < 0.5$ mm. Muons are characterised as signal muons if they have a higher transverse momentum, $p_{\mathrm{T}} > 20$ GeV, and satisfy the "GradientLoose" isolation requirement [81], as well as a further transverse impact parameter restriction $|d_0|/\sigma(d_0) < 3$. Signal muons are used in leptonic control regions, as described in Section 6.2. Muon reconstruction and identification efficiencies in simulated samples are corrected with factors evaluated by a data-MC comparison [82].

To resolve the reconstruction ambiguities between electrons, muons and jets, an overlap removal procedure is applied to baseline objects. First, any electron sharing an ID track with a muon is rejected. If it shares the same ID track with another electron, the one with lower p_{T} is discarded. Next, photons with $\Delta R < 0.4$ relative to an electron or a muon are discarded. Subsequently, non-b-tagged jets are rejected if they lie within $\Delta R = 0.2$ of an electron or if the jet has no more than three tracks with $p_{\mathrm{T}} > 500$ MeV, or contains an ID track matched to a muon such that $p_{\mathrm{T}}^{\mathrm{jet}} < 2p_{\mathrm{T}}^{\mu}$ and the muon track has more than 70% of the sum of the transverse momenta of all tracks in the jet, such that the jet resembles radiation from the muon. Finally, electrons or muons with $\Delta R < 0.4$ from a surviving jet are eliminated and jets with $\Delta R < 0.4$ from photons are removed.

The missing transverse momentum, $E_{\mathrm{T}}^{\mathrm{miss}}$, is defined as the magnitude of the negative vector sum of the transverse momenta of baseline electrons and muons, photons and jets, which pass an overlap removal procedure, based on removing duplicated energy contributions and therefore distinct from that used for jet/lepton disambiguation. A "soft term" is added to recover the contributions from other low-p_{T} particles [83]. The soft term is constructed from all tracks that are not associated with any of the preceding objects, and that are associated with the hard scatter vertex. In this way, the missing transverse momentum is adjusted for the best calibration of the leptons, photons and jets, while maintaining pile-up robustness in the soft term.

The $E_{\mathrm{T}}^{\mathrm{miss}}$ significance $\mathcal{S}(E_{\mathrm{T}}^{\mathrm{miss}})$ is defined to test the hypothesis that the total transverse momentum carried by non-interacting particles is equal to zero against the hypothesis that it is different from zero. It quantifies the degree to which the measured $E_{\mathrm{T}}^{\mathrm{miss}}$ is inconsistent with originating purely from fluctuations and mismeasurements. A large value indicates that the $E_{\mathrm{T}}^{\mathrm{miss}}$ genuinely originates from non-interacting particles. In this search, the variable $\mathcal{S}(E_{\mathrm{T}}^{\mathrm{miss}})$ characterises the $E_{\mathrm{T}}^{\mathrm{miss}}$ based on the p_{T}, p_{T} resolution, and ϕ resolution of all objects in the event and is defined as [18]:

$$\mathcal{S}(E_{\mathrm{T}}^{\mathrm{miss}}) = \frac{E_{\mathrm{T}}^{\mathrm{miss}}}{\sqrt{\sigma_{\mathrm{L}}^2(1-\rho_{\mathrm{LT}}^2)}}. \tag{1}$$

In this definition, σ_{L} is the total expected longitudinal resolution of all objects in the event as a function of the p_{T} of each object. Likewise, ρ_{LT} is the correlation factor between all longitudinal and transverse object resolutions. The resolution on the soft term is taken to be a fixed 8.9 GeV in each of the transverse coordinates. Each jet resolution is further modified by the probability that the jet is a pile-up jet mistakenly tagged as being from the hard scatter interaction, parameterised in p_{T}, η and JVT. By individually accounting for these resolutions, this "object-based" $\mathcal{S}(E_{\mathrm{T}}^{\mathrm{miss}})$ definition captures the response of the ATLAS detector and reconstruction algorithms better than the simpler $\mathcal{S}(E_{\mathrm{T}}^{\mathrm{miss}})$ proxies used in previous searches (such as in Ref. [16]).

5 Event selection

Target signal events for this analysis are characterised by a large jet multiplicity, beyond that generated by high cross-section SM processes, combined with an $E_{\mathrm{T}}^{\mathrm{miss}}$ value that is significantly larger than that expected purely from detector resolution and mismeasurement effects. Several signal regions are defined that select a minimum jet multiplicity and further require a large value of $\mathcal{S}(E_{\mathrm{T}}^{\mathrm{miss}})$.

The common selection of events for the signal regions is as follows. Events are rejected if no primary vertex is reconstructed. To limit the contribution of SM background processes in which neutrinos are produced via the decay $W \to \ell\nu$, leading to significant $E_{\mathrm{T}}^{\mathrm{miss}}$, events containing any baseline electron or muon with $p_{\mathrm{T}} > 10$ GeV surviving the overlap removal are rejected.

Biases in the $E_{\mathrm{T}}^{\mathrm{miss}}$ due to pile-up jets surviving the JVT selection are removed by excluding events for which a jet j with 60 GeV$< p_{\mathrm{T}} <$ 70 GeV and JVT < 0.2 lies opposite to the $E_{\mathrm{T}}^{\mathrm{miss}}$ vector in ϕ ($\Delta\phi(j, E_{\mathrm{T}}^{\mathrm{miss}}) > 2.2$). Likewise, events are rejected if they contain a jet with $p_{\mathrm{T}} > 50$ GeV and $|\eta| < 2.0$ pointing in $\eta - \phi$ towards regions in which tile calorimeter modules were disabled.

Subsequently, restrictions on the jet multiplicity N_{jet} are imposed; only jets with $p_{\mathrm{T}} > 50$ (80) GeV and $|\eta| < 2.0$ are considered as *signal jets* and therefore used in the N_{jet} selection. These selections are abbreviated as j50 (j80), for which the corresponding jet multiplicities are denoted N_{jet}^{50} (N_{jet}^{80}). The lower and higher jet p_{T} thresholds allow to probe a variety of potential SUSY mass spectra and ensure that the corresponding trigger selections have efficiencies that match to within 2% in simulation and in data.

A threshold of $\mathcal{S}(E_{\mathrm{T}}^{\mathrm{miss}}) > 5$ is the last element of the common selection. This criterion eliminates the vast majority of SM multijet and other background events with low $E_{\mathrm{T}}^{\mathrm{miss}}$, while retaining sensitivity to a broad range of potential signals.

Motivated by the likelihood of heavy-flavour jets being produced from cascade decays, events are classified by their b-jet multiplicity. Events passing the common selection may then be categorised according to three classes depending on whether they satisfy $N_{b\text{-jet}} = 0$, $N_{b\text{-jet}} = 1$ or $N_{b\text{-jet}} \geq 2$.

Should SUSY particles be produced and decay through a long decay chain, or provide enough kinetic energy to significantly boost heavy particles such as top quarks or SM electroweak bosons, signal events might be characterised not only by an unusually large jet multiplicity but also by the formation of large-radius jets with high masses. The kinematic structure of SM events, by contrast, does not produce a high rate of events containing large-radius jets with a mass greater than the top quark mass. On this basis, the selection variable M_{J}^{Σ} is defined to be the sum of the masses $m_j^{R=1.0}$ of the large-radius jets

$$M_{\mathrm{J}}^{\Sigma} = \sum_j m_j^{R=1.0}$$

where the sum is over the large-radius jets that satisfy $p_{\mathrm{T}}{}_j^{R=1.0} > 100$ GeV and $|\eta_j^{R=1.0}| < 1.5$, as described in Section 4. After the common selection and $N_{b\text{-jet}}$ classification, selected events may be further partitioned into three M_{J}^{Σ} bins:

- $M_{\mathrm{J}}^{\Sigma} \leq 340$ GeV;
- 340 GeV $< M_{\mathrm{J}}^{\Sigma} \leq 500$ GeV;
- $M_{\mathrm{J}}^{\Sigma} > 500$ GeV.

Selection criterion	Selection ranges	
Jet multiplicity, N_{jet}	$N_{\text{jet}}^{50} \geq \{8, 9, 10, 11, 12\}$	$N_{\text{jet}}^{80} \geq 9$
Trigger thresholds	2015-2016: 6 jets, $E_{\text{T}} > 45$ GeV	2015: 5 jets, $E_{\text{T}} > 70$ GeV 2016: 5 jets, $E_{\text{T}} > 65$ GeV
	2017-2018: 7 jets, $E_{\text{T}} > 45$ GeV	2017-2018: 5 jets, $E_{\text{T}} > 70$ GeV
Lepton veto	0 baseline leptons, $p_{\text{T}} > 10$ GeV	
$E_{\text{T}}^{\text{miss}}$ significance, $\mathcal{S}(E_{\text{T}}^{\text{miss}})$	$\mathcal{S}(E_{\text{T}}^{\text{miss}}) > 5.0$	

Table 1: Summary of common selections prior to the categorisations based on $N_{b\text{-jet}}$ and M_{J}^{Σ}.

As the bin boundaries are at approximately twice and three times the top quark mass, the residual irreducible backgrounds remaining in the higher M_{J}^{Σ} bins are respectively top quark pair production in association with vector bosons and processes with four top quarks, both of which have a very small rate.

The subselections in $N_{b\text{-jet}}$ and M_{J}^{Σ} are used in two sub-analyses. First, a set of multi-bin signal selections is defined to improve the exclusion reach in the absence of an observed excess. Starting from the common selections, shown in Table 1, for $N_{\text{jet}}^{50} \geq 8$, the selected events are partitioned by $N_{b\text{-jet}}$ and M_{J}^{Σ} according to the thresholds above, defining nine statistically independent bins, as shown in Table 2. The same subdivision is applied for events satisfying the $N_{\text{jet}}^{50} \geq 9$ and $N_{\text{jet}}^{50} \geq 10$ common selections. The statistical analyses of the three different N_{jet}^{50} selections are performed separately since the selections are not statistically independent. For example one of the nine bins in the 8-jet selection (e.g. $N_{b\text{-jet}} = 0$, $M_{\text{J}}^{\Sigma} > 500$) includes all events in the corresponding bin for the 9- and 10-jet selections. The inputs to the statistical analysis include also validation regions (VRs) and control regions (CRs), further discussed in Section 6.

Additionally, an ensemble of single-bin regions is defined making use of inclusive selections in $N_{b\text{-jet}}$ and M_{J}^{Σ}, which are designed to reject the SM hypothesis with high confidence, should new physics be present. Following an optimisation procedure to maximise coverage over the benchmark signal models, the signal regions defined in Table 3 were selected. To give an indication of their relevance, the two-step gluino cascade decay motivates the `SR-10ij50-0ib-MJ340` and `SR-10ij50-0ib-MJ500` regions while the `SR-9ij50-0ib-MJ340` and `SR-10ij50-1ib-MJ500` regions are optimised for sensitivity to gluino decays to top quarks. The `SR-10ij50-1ib-MJ500` selection also provides the best sensitivity to RPV gluino decays.

If an excess of data is observed over the background predictions, its significance can be quantified in the single-bin regions. If on the contrary the data are consistent with the background only hypothesis, signal models are excluded based on the constraint achieved by whichever signal region is expected to be most sensitive to the model, whether it is a single- or multi-bin selection.

6 Background estimation

The signal selection in this analysis demands higher jet multiplicities than can practically be generated with fixed-order multi-leg matrix element MC generators for most SM background processes. The kinematic

Signal region	N_{jet}^{50}	$N_{b\text{-jet}}$	M_{J}^{Σ} (GeV)
SR-8ij50 multi-bin	≥8	= 0, = 1, ≥ 2	(0, 340], (340, 500], (500, ∞)
SR-9ij50 multi-bin	≥9		
SR-10ij50 multi-bin	≥10		

Table 2: Signal region subdivisions for the multi-bin fit in the {8,9,10}ij50 analysis channels. The selections on these variables apply to the signal regions as well as to the multijet template and validation regions described later in Section 6. For each inclusive jet multiplicity fit, nine regions are generated combining the $N_{b\text{-jet}}$ and M_{J}^{Σ} selections.

Signal region	N_{jet}^{50}	N_{jet}^{80}	$N_{b\text{-jet}}$	M_{J}^{Σ} (GeV)
SR-8ij50-0ib-MJ500	≥8	-	-	≥500
SR-9ij50-0ib-MJ340	≥9	-	-	≥340
SR-10ij50-0ib-MJ340	≥10	-	-	≥340
SR-10ij50-0ib-MJ500	≥10	-	-	≥500
SR-10ij50-1ib-MJ500	≥10	-	≥1	≥500
SR-11ij50	≥11	-	-	-
SR-12ij50-2ib	≥12	-	≥2	-
SR-9ij80	-	≥9	-	-

Table 3: Summary of signal region criteria for single-bin selections. The requirements in multiplicity and M_{J}^{Σ} are inclusive in all cases. A dash ('-') indicates that there is no requirement applied to the corresponding variable. The requirement $\mathcal{S}(E_{\text{T}}^{\text{miss}}) > 5$ is applied to all bins.

requirements also challenge the parton shower approximations that are used to obtain higher multiplicities than are possible in fixed order calculations. For this reason the analysis has been designed in a manner that allows the expected yields in the signal regions for each of the most important backgrounds to be determined either from fully data-driven methods or by using measurements of ATLAS data to calibrate and to confirm the predictions of the MC simulations.

Three different broad classes of backgrounds are identified, and a different strategy is employed for each.

The first class of background is multijet production through QCD processes in which detector resolution effects produce an apparent momentum imbalance even in the absence of any true $E_{\text{T}}^{\text{miss}}$. This class includes any contribution to the $E_{\text{T}}^{\text{miss}}$ from neutrinos when semi-leptonic decays of b- and c-hadrons are present in those jets. The probability distribution of jet mismeasurement from either source can be measured with high statistical precision from data in lower jet multiplicity events. The distribution of $\mathcal{S}(E_{\text{T}}^{\text{miss}})$ is observed to be almost independent of the jet multiplicity, and so the expected yield in each signal region can be determined using a data-driven background template of $\mathcal{S}(E_{\text{T}}^{\text{miss}})$ extracted from lower jet multiplicity data. Section 6.1 describes this method fully.

The second class of backgrounds consists of processes which contain true momentum imbalance caused by the production of neutrinos in association with charged leptons (excluding semi-leptonic b- and c-hadron

decays, which fall in the first class). The dominant backgrounds in this second class are $t\bar{t}$ and W+jets production. For such backgrounds auxiliary measurements of the data in control regions (CRs) are used to normalise the predictions from MC simulation. This control region approach is described in detail in Section 6.2.

The third class comprises subdominant backgrounds such as leptonically-decaying Z bosons and associated jets (Z+jets), single-top-quark production, diboson production of WW, WZ, or ZZ, and the production of $t\bar{t}$ in association with heavier particles – this final item covers the production of three or four top quarks, $t\bar{t}+W$, $t\bar{t}+Z$, and $t\bar{t}+WW$ production, and is collectively referred to as '$t\bar{t}+X$'. The expected yields from these backgrounds are found to be sufficiently small that they may be estimated with adequate precision from MC simulation alone.

The final determination of each of the first two classes of backgrounds is obtained using a simultaneous fit including control regions, as described in Section 6.3.

6.1 Multijet background

The analysis is designed such that a data-driven method can be used for the estimation of the dominant multijet background. This technique relies on the approximate invariance of the multijet $\mathcal{S}(E_{\mathrm{T}}^{\mathrm{miss}})$ distribution with respect to changes to the jet multiplicity. The procedure is also referred to as the *multijet template estimate* and is schematically shown in Figure 2, which illustrates various template regions (TRs) used to extract the prediction.

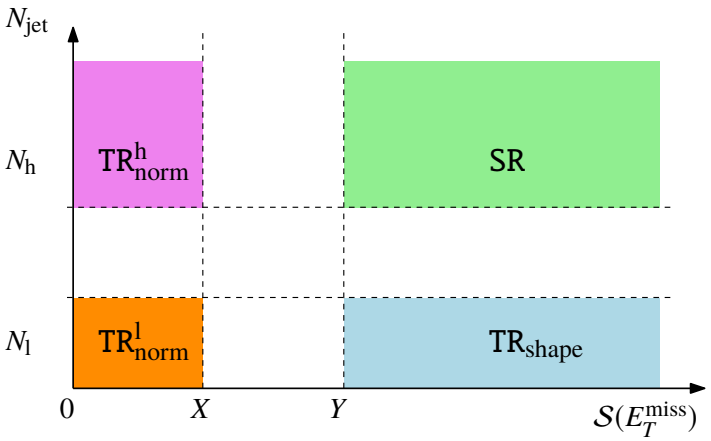

Figure 2: Schematic of the kinematic regions used in the template method for the multijet background. SR represents any signal region, while the three TR variations are regions used to extract and normalise the corresponding background prediction.

The predicted multijet background yield in a region $\hat{N}[a < \mathcal{S}(E_{\mathrm{T}}^{\mathrm{miss}}) < b]$ with high jet multiplicity (N_{h}) and $\mathcal{S}(E_{\mathrm{T}}^{\mathrm{miss}})$ in the range (a, b) is obtained from the measured yield $N_{\mathrm{TR}_{\mathrm{shape}}}$ in a lower jet multiplicity (N_{l}) template region $\mathrm{TR}_{\mathrm{shape}}$ through the relation

$$\hat{N}[a < \mathcal{S}(E_{\mathrm{T}}^{\mathrm{miss}}) < b] = \frac{N_{\mathrm{TR}^{\mathrm{h}}_{\mathrm{norm}}}}{N_{\mathrm{TR}^{\mathrm{l}}_{\mathrm{norm}}}} N_{\mathrm{TR}_{\mathrm{shape}}}[a < \mathcal{S}(E_{\mathrm{T}}^{\mathrm{miss}}) < b]. \tag{2}$$

In this equation, the regions for template normalisation $\texttt{TR}^{\text{l}}_{\text{norm}}$ and $\texttt{TR}^{\text{h}}_{\text{norm}}$, at lower and higher jet multiplicity respectively, require $\mathcal{S}(E_{\text{T}}^{\text{miss}}) < 2$ in order to reduce signal and leptonic background contamination. The fraction of signal contamination for non-excluded parameter values in the target models is found to range from $< 0.1\%$ to 10% depending on the region.

The multijet yields in the template regions $\texttt{TR}_{\text{shape}}$, $\texttt{TR}^{\text{l}}_{\text{norm}}$ and $\texttt{TR}^{\text{h}}_{\text{norm}}$ are extracted by subtracting the leptonic background prediction from the yield in data. For signal regions requiring $N^{50}_{\text{jet}} \geq 8 - 12$, the $\texttt{TR}^{\text{l}}_{\text{norm}}$ and $\texttt{TR}_{\text{shape}}$ are defined using events with $N^{50}_{\text{jet}} = 7$. The criterion $N^{80}_{\text{jet}} = 6$ defines the corresponding template regions for the signal region selecting events with $N^{80}_{\text{jet}} \geq 9$. The $\texttt{TR}^{\text{h}}_{\text{norm}}$ selection requires the same jet multiplicity as the corresponding signal region.

A residual dependence of the multijet template estimate on event kinematics has previously been observed [15]. This secondary dependence is addressed by applying the template method differentially in bins of the total scalar sum of jet transverse momenta $H_{\text{T}} = \sum_{j \in \text{jets}} p_{\text{T}\,j}$, where $p_{\text{T}\,j} > 40\,\text{GeV}$. The H_{T} bin ranges are chosen dynamically to ensure good statistical precision in each bin. The effect of changing the binning on the background estimate is included in the systematic uncertainty. For each signal region bin, the template estimate is extracted after applying the same M_{J}^{Σ} and $N_{b\text{-jet}}$ selections to all relevant template regions. Residual inaccuracies due to the N_{jet} extrapolation and potential mismodelling of the simulated backgrounds in the template regions are corrected in a control region (QCR) defined in the range $3 < \mathcal{S}(E_{\text{T}}^{\text{miss}}) < 4$, and at the same jet multiplicity as the signal region. The yield in each QCR is used as input to the simultaneous fit described in Section 6.3.

To verify the accuracy of the multijet background prediction two sets of validation regions are defined. These correspond to the two dimensions in which the background prediction is extrapolated:

- $\texttt{VR}_{N_{\text{jet}}}$ is defined at a jet multiplicity below that of the signal region, and tests the extrapolation in $\mathcal{S}(E_{\text{T}}^{\text{miss}})$;
- $\texttt{VR}_{\mathcal{S}(E_{\text{T}}^{\text{miss}})}$ instead is defined in an intermediate $\mathcal{S}(E_{\text{T}}^{\text{miss}})$ range between the QCR and the signal region, specifically $4 < \mathcal{S}(E_{\text{T}}^{\text{miss}}) < 5$, and tests the extrapolation in N_{jet}.

For the SR-9ij80 signal region, the $\texttt{VR}_{N_{\text{jet}}}$ requires $N^{80}_{\text{jet}} = 7$, a multiplicity between the template regions and the signal region selection. An intermediate jet multiplicity region is not available for the j50 selections, as the SR-8ij50 regions are adjacent to the template regions. Instead, the $\texttt{VR}_{N_{\text{jet}}}$ requires $N^{50}_{\text{jet}} = 7$, and the test is performed on a template extracted from data with $N^{50}_{\text{jet}} = 6$, selected with a prescaled trigger. The template region $\mathcal{S}(E_{\text{T}}^{\text{miss}})$ and N_{jet} requirements are summarised together with the QCR and VR requirements in Table 4 and Table 5. Example distributions of $\mathcal{S}(E_{\text{T}}^{\text{miss}})$ in the lower-jet multiplicity VRs are shown in Figure 3.

$\mathcal{S}(E_{\text{T}}^{\text{miss}})$ range	0-2	2-3	3-4	4-5	> 5
$N^{80}_{\text{jet}} = 5$	$\texttt{TR}^{\text{l}}_{\text{norm}}$	–	–	–	$\texttt{TR}_{\text{shape}}$
$N^{80}_{\text{jet}} = 6$	–	–	–	–	$\texttt{VR}_{N_{\text{jet}}}$
$N^{80}_{\text{jet}} \geq 9$	$\texttt{TR}^{\text{h}}_{\text{norm}}$	–	QCR	$\texttt{VR}_{\mathcal{S}(E_{\text{T}}^{\text{miss}})}$	SR

Table 4: Illustration of the main multijet template, control and validation regions in N_{jet} and $\mathcal{S}(E_{\text{T}}^{\text{miss}})$ corresponding to the SR-9ij80 signal region. The template regions used to derive predictions in the control and validation regions are not shown.

$\mathcal{S}(E_{\mathrm{T}}^{\mathrm{miss}})$ range	0-2	2-3	3-4	4-5	> 5
$N_{\mathrm{jet}}^{50} = 6$, prescaled data	$\mathrm{TR}_{\mathrm{norm}}^{\mathrm{l,prescale}}$	–	–	–	$\mathrm{TR}_{\mathrm{shape}}^{\mathrm{prescale}}$
$N_{\mathrm{jet}}^{50} = 7$, full dataset	$\mathrm{TR}_{\mathrm{norm}}^{\mathrm{h,prescale}}$	–	–	–	$\mathrm{VR}_{N_{\mathrm{jet}}}$
$N_{\mathrm{jet}}^{50} = 7$, full dataset	$\mathrm{TR}_{\mathrm{norm}}^{\mathrm{l}}$	–	–	–	$\mathrm{TR}_{\mathrm{shape}}$
$N_{\mathrm{jet}}^{50} \geq 8$, full dataset	$\mathrm{TR}_{\mathrm{norm}}^{\mathrm{h}}$	–	QCR	$\mathrm{VR}_{\mathcal{S}(E_{\mathrm{T}}^{\mathrm{miss}})}$	SR

Table 5: Illustration of the main multijet template, control and validation regions in N_{jet} and $\mathcal{S}(E_{\mathrm{T}}^{\mathrm{miss}})$ corresponding to the `j50` signal regions. The template regions needed to derive predictions in the control and $\mathrm{VR}_{\mathcal{S}(E_{\mathrm{T}}^{\mathrm{miss}})}$ regions are not shown. For the rows labeled "prescaled data", a six-jet trigger was used that collected only a fraction of the Run 2 data. The superscript "`prescale`" is used to indicate the template regions used to predict the $\mathrm{VR}_{N_{\mathrm{jet}}}$ background using prescaled data.

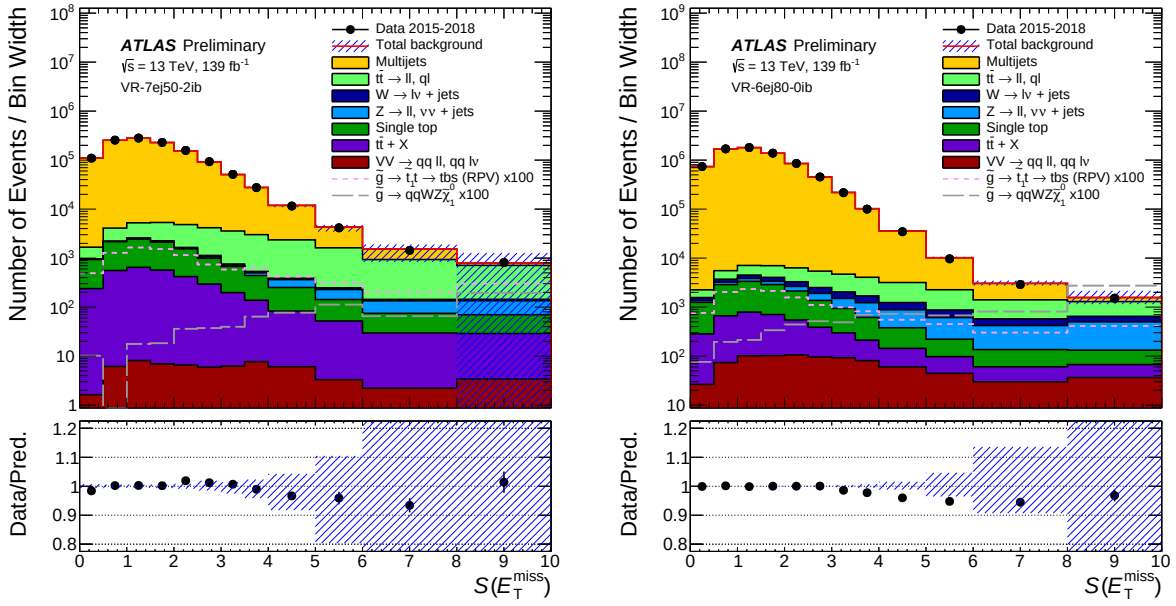

(a) $N_{\mathrm{jet}}^{50} = 7$, $N_{b\text{-jet}} \geq 2$

(b) $N_{\mathrm{jet}}^{80} = 6$, $N_{b\text{-jet}} \geq 0$

Figure 3: Distributions of the $\mathcal{S}(E_{\mathrm{T}}^{\mathrm{miss}})$ for events in two of the validation regions. The upper panel shows the absolute yields for data (black points) and all background subcomponents (histograms), with the combination of statistical and systematic uncertainties shown by the hatched areas. The yields for two benchmark signal models are overlaid, representing 1.6 TeV gluinos decaying to W and Z bosons and a 100 GeV neutralino via intermediate gauginos (long dashed histogram) or instead to tbs/tbd via a 600 GeV top squark through an R-parity violating (RPV) coupling (short dashed histogram). Signal yields have been scaled by a factor of 100 for visibility. The lower panel shows the ratio of the data yields to the total SM prediction.

6.2 Leptonic backgrounds

The SM processes which produce multijet events with one or more leptons are categorised as *leptonic* backgrounds. Although events containing charged leptons (e or μ) are excluded from the signal regions, it is still possible for leptonic backgrounds to contaminate them. The veto only applies to events containing electrons and muons, hence hadronically decaying τ-leptons (originating from top quark or W boson decays) remain a source of background. Such τ-leptons are treated as jets within this analysis, so may contribute to the jet count if they have sufficient p_{T}, and the momentum lost through any associated neutrinos can also cause these events to enter the signal regions. Additionally, there are cases where the electrons or muons may fall outside of the detector acceptance, or be misreconstructed in the detector, increasing the $E_{\mathrm{T}}^{\mathrm{miss}}$ of the event.

The two largest leptonic backgrounds are from leptonically and semi-leptonically decaying $t\bar{t}$, and leptonically-decaying W bosons produced in association with jets. The estimation of these backgrounds employs the MC simulations described in Section 3. To reduce normalisation and modelling uncertainties the background predictions are normalised to data using CRs.

The control regions are designed to be kinematically similar to signal regions, yet non-overlapping with them. They are designed to enhance the contributions from particular backgrounds, in order to measure those backgrounds cleanly, while being comparatively sparse in signal contamination. Statistical orthogonality between the signal regions and the leptonic CRs is achieved by requiring exactly one electron or muon in the event. To reduce statistical uncertainties, each $N_{\mathrm{jet}} \geq m$ signal region has a corresponding ($N_{\mathrm{jet}} \geq m-1$) control region, except in the case of signal regions with an $N_{\mathrm{jet}}^{50} \geq 8$ requirement, where there are sufficiently large yields in the control region to match the signal region $N_{\mathrm{jet}} \geq m$ requirement. In the control regions with higher jet multiplicity requirements the $\mathcal{S}(E_{\mathrm{T}}^{\mathrm{miss}})$ threshold is reduced, as shown in Table 6, to increase the statistical precision. This is not expected to bias the background normalisation, as the agreement between data and simulated yields does not change systematically as a function of $\mathcal{S}(E_{\mathrm{T}}^{\mathrm{miss}})$.

Two leptonic control regions are defined for each signal region: the first (`WCR`) includes a b-jet veto to enhance the contribution of W+jets backgrounds, and the second (`TCR`) requires at least one b-jet in the event, enriching the region with the $t\bar{t}$ background. The signal-region p_{T} thresholds on the jets also apply to the corresponding control regions. To simulate the effect of τ-leptons being reconstructed as jets in the signal regions, electrons and muons are also included as jets, for the purpose of the corresponding CR selection, provided that they pass the same p_{T} and $|\eta|$ requirements as the jets in the event. Finally, an upper bound on the transverse mass[2] computed with the lepton and $E_{\mathrm{T}}^{\mathrm{miss}}$ is applied at 120 GeV in order to reduce contributions from signal processes. This variable has a kinematic endpoint at the W mass for leptonically-decaying on-shell W bosons, but has no such bound when the lepton and $E_{\mathrm{T}}^{\mathrm{miss}}$ originate from different decays. The control region definitions are summarised in Table 7, and the different $\mathcal{S}(E_{\mathrm{T}}^{\mathrm{miss}})$ thresholds are indicated in Table 6.

Additional requirements are placed on M_{J}^{Σ} for the control regions in the same manner as for the corresponding signal region selections. In the case of the single-bin selections (Table 3), the same threshold is applied. For multi-bin selections, the control regions have three bins, corresponding to the same M_{J}^{Σ} thresholds, as shown in Table 8.

The `WCR` and `TCR` are used as inputs to a fit that applies normalisation corrections to the $t\bar{t}$ and W+jets background components, as described in Section 6.3.

[2] The transverse mass is defined as $m_{\mathrm{T}} = \sqrt{2p_{\mathrm{T}}^{\ell}E_{\mathrm{T}}^{\mathrm{miss}}\left[1-\cos\left(\Delta\phi(\vec{p_{\mathrm{T}}}^{\,\ell},\vec{E}_{\mathrm{T}}^{\mathrm{miss}})\right)\right]}$, where p_{T}^{ℓ} is the lepton p_{T}.

N_{jet}^{50}	N_{jet}^{80}	$\mathcal{S}(E_{\text{T}}^{\text{miss}})$ selection
≥8	–	>5
≥9	–	>4
≥10, ≥11	≥8	>4

Table 6: Summary of the individual $\mathcal{S}(E_{\text{T}}^{\text{miss}})$ selections for the leptonic control regions.

Selection criterion	Selection ranges
Lepton multiplicity	Exactly one signal e or μ remaining after overlap removal
Lepton p_{T}	> 20 GeV
m_{T} (ℓ,$E_{\text{T}}^{\text{miss}}$)	< 120 GeV
Trigger	Same as signal regions
Jet p_{T}, $\lvert\eta\rvert$	Same as signal regions
N_{jet} (including lepton)	≥ 8, for N_{jet}^{50} ≥ 8 signal regions; ≥ ($N_{\text{jet}}^{\text{SR}}$ − 1), otherwise
$N_{b\text{-jet}}$	= 0 (WCR), ≥ 1 (TCR)
M_{J}^{Σ}	Same as signal regions
$\mathcal{S}(E_{\text{T}}^{\text{miss}})$	Table 6

Table 7: Summary of the selections used to define the leptonic control regions.

8, 9, 10ij50 CR definitions	$N_{b\text{-jet}} = 0$	$N_{b\text{-jet}} \geq 1$
$M_{\text{J}}^{\Sigma} \leq 340$ GeV	WCR1	TCR1
340 GeV $< M_{\text{J}}^{\Sigma} \leq 500$ GeV	WCR2	TCR2
$M_{\text{J}}^{\Sigma} > 500$ GeV	WCR3	TCR3

Table 8: Control region subdivisions for the background fits for multi-bin signal selections.

6.3 Background normalisation corrections

Background estimates in the signal region are made more accurate by employing a background likelihood fit based on the control regions, using the methods described in Ref. [84]. By means of this fit, the raw estimated yields for the major background components, including the multijet $t\bar{t}$, and W+jets processes, are corrected for mismodelling. For the other background processes, which contribute on the order of 1% of the SR yields, the nominal MC predictions are used directly. The multijet background, while estimated using a data-driven procedure, is incorporated in the simultaneous fit due to the dependence of the template prediction on the subtraction of other backgrounds which include the simulated $t\bar{t}$ and W+jets estimates. Besides correcting for any residual mismodelling, fitting the multijet component handles the correlations between the systematic uncertainties on the different background components consistently.

In the case of the single-bin regions (Table 3), the normalisations of the background components are

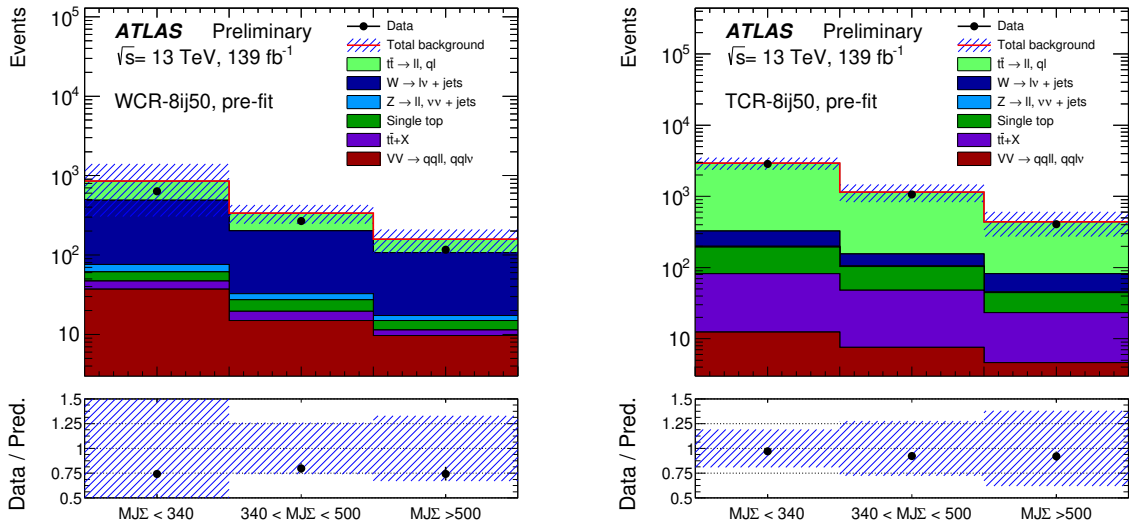

(a) WCR, pre-fit

(b) TCR, pre-fit

Figure 4: Pre-fit yields in the (a) W+jets and (b) $t\bar{t}$ background normalisation regions for the SR-8ij50 multi-bin analysis. The upper panel shows the absolute yields for data (black points) and all background subcomponents (histograms), with the combination of statistical and systematic uncertainties shown by the hatched areas. The lower panel shows the ratio of the data yields to the total SM prediction.

allowed to vary within their nominal uncertainties, described in Section 6.4. For the multi-bin analysis channels (Table 2), the additional information available to the fit permits a reduction in the uncertainties, as well as a modification of the event yields to better accommodate the control region measurements. To avoid artificially constraining systematic uncertainties in the background fit due to the high statistical precision, the multijet normalisation region QCR is limited to a single bin, $N_{b\text{-jet}} \geq 0$, $M_{\mathrm{J}}^{\Sigma} \geq 0$.

For illustration, the pre-fit yields for the SR-8ij50 leptonic CRs are shown in Figure 4, demonstrating the extent of the observed mismodelling in the W+jets and $t\bar{t}$ normalisation. The fitted normalisation factors are summarised for all signal selections in Figure 5, and are found to be consistent across the wide range of jet multiplicities probed.

Figure 6 shows the background modelling in the validation regions $\mathrm{VR}_{N_{\mathrm{jet}}}$ and $\mathrm{VR}_{\mathcal{S}(E_{\mathrm{T}}^{\mathrm{miss}})}$ for the SR-8ij50 multi-bin analysis. Considering uncertainties, the data yields are in agreement with the predictions after applying the background normalisation factors. Similar levels of agreement are found for the single-bin signal regions, as can be seen in Figure 7. In the $\mathrm{VR}_{\mathcal{S}(E_{\mathrm{T}}^{\mathrm{miss}})}$, there is a tendency for the background predictions to mildly overshoot the data, at the level of 10%. This is due to residual kinematic correlations causing the $\mathcal{S}(E_{\mathrm{T}}^{\mathrm{miss}})$ distribution not to be entirely independent of the jet multiplicity. Applying flavour-tagging and jet mass selections alters these correlations. In the validation and signal regions, an uncertainty is applied based on the largest observed non-closure at lower jet multiplicities or smaller $\mathcal{S}(E_{\mathrm{T}}^{\mathrm{miss}})$ values, and is found to cover the observed discrepancies.

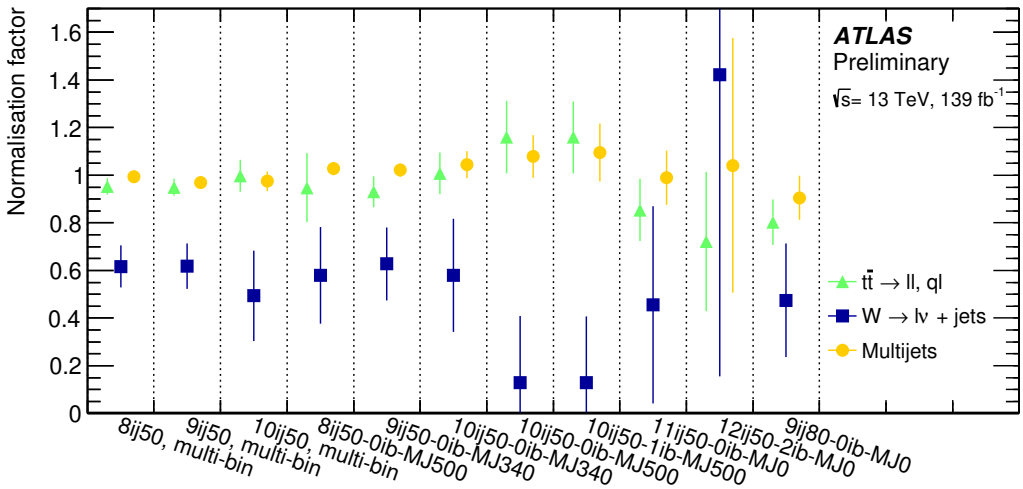

Figure 5: Summary of the fitted normalisation factors for the $t\bar{t}$, W+jets and multijet backgrounds in all signal regions. The error bars indicate the combination of statistical and systematic uncertainties on the corresponding factors. Two pairs of SRs, namely the `SR-8ij50` and `SR-9ij50` multi-bin regions and the `SR-10ij50-0ib-MJ500` and `SR-10ij50-1ib-MJ500` single-bin regions share leptonic control regions, and therefore have highly correlated normalisation factors for the W+jets and $t\bar{t}$ background components.

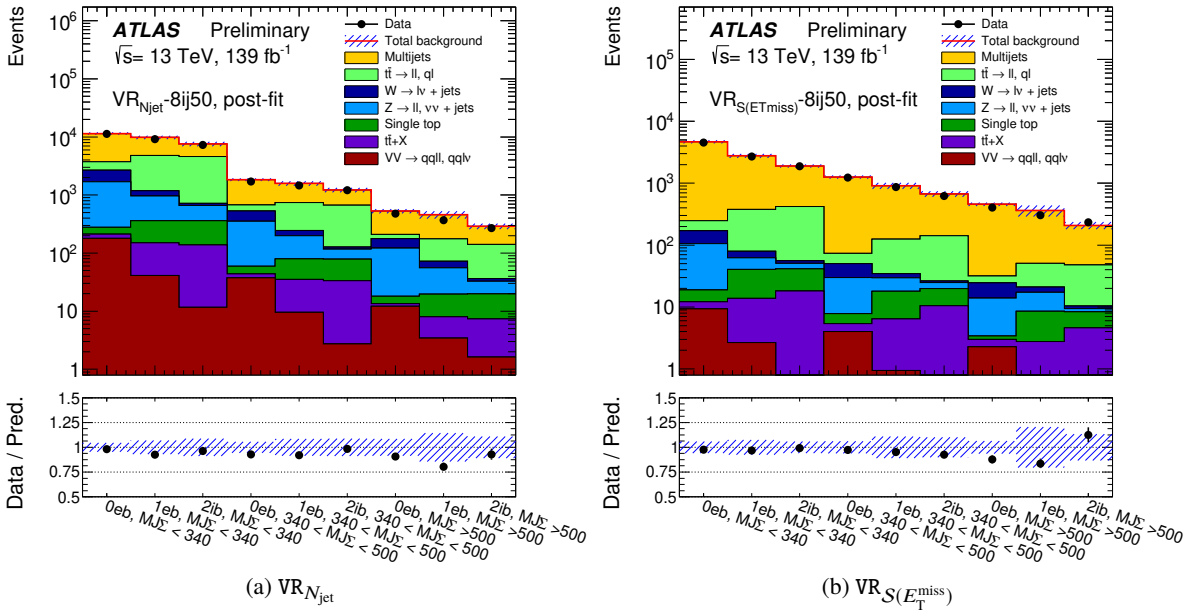

(a) $\mathrm{VR}_{N_{\mathrm{jet}}}$ (b) $\mathrm{VR}_{\mathcal{S}(E_{\mathrm{T}}^{\mathrm{miss}})}$

Figure 6: Post-fit event yields in validation regions for the `SR-8ij50` multi-bin analysis. The upper panel shows the absolute yields for data (black points) and all background subcomponents (histograms), with the combination of statistical and systematic uncertainties shown by the hatched areas. The lower panel shows the ratio of the data yields to the total SM prediction.

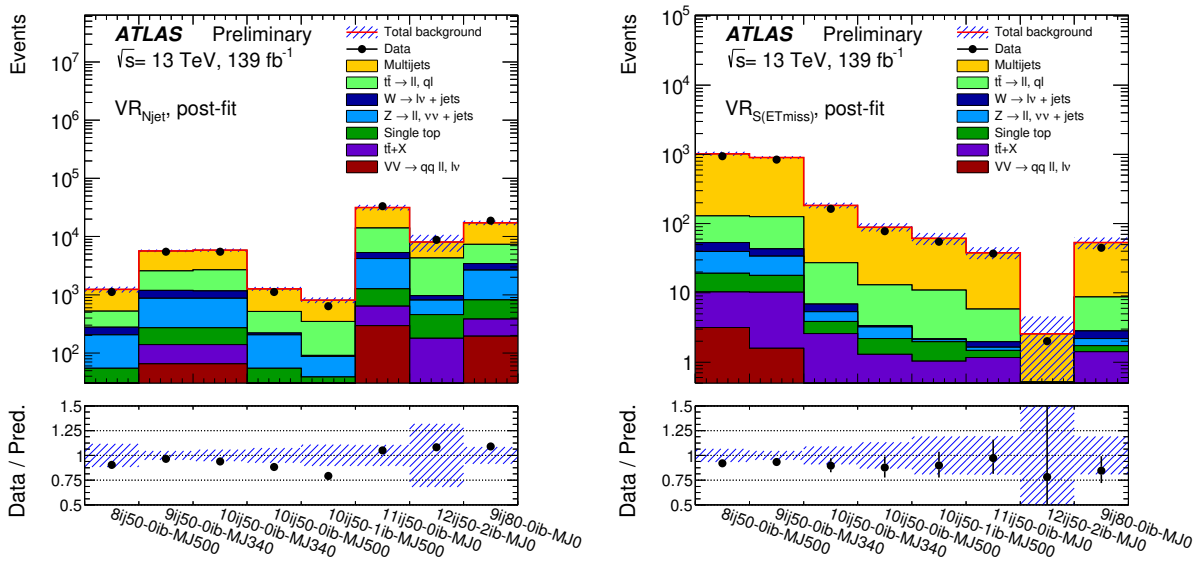

(a) $\mathrm{VR}_{N_{\mathrm{jet}}}$ (b) $\mathrm{VR}_{\mathcal{S}(E_{\mathrm{T}}^{\mathrm{miss}})}$

Figure 7: Post-fit event yields in validation regions summarised for all single-bin signal regions. The upper panel shows the absolute yields for data (black points) and all background subcomponents (histograms), with the combination of statistical and systematic uncertainties shown by the hatched areas. The lower panel shows the ratio of the data yields to the total SM prediction.

6.4 Systematic uncertainties

Systematic uncertainties from the following sources are assessed on the background predictions. Experimental systematic uncertainties chiefly include uncertainties on the energy or momentum scales of reconstructed jets and leptons or the missing transverse momentum, as well as the uncertainty on the total integrated luminosity and the magnitude of pile-up corrections. Theoretical uncertainties are assessed by varying the scales (renormalisation, factorisation, resummation, shower matching) at which cross-sections are calculated or by comparison of an ensemble of matrix element and parton shower programmes used to generate the predictions. Each source of theoretical uncertainty is correlated across the signal, control and validation region selections, but assessed separately for each background process.

Additional uncertainties account for potential inaccuracies in the data-driven multijet estimate. The effects of residual kinematic correlations are estimated by modifying the H_{T}-binning procedure used in the multijet estimate. A comparison of the nominal prediction to an alternative prediction assuming an increased resolution for flavour-tagged jets measured in data is used to estimate the impact of different flavour composition in the template and signal regions. Finally, a conservative uncertainty is assessed based on the observed non-closure of the prediction in validation regions.

The dominant sources of systematic uncertainty are listed in Table 9. The total uncertainty on the predicted signal region yield is in the range 6–14% for the multi-bin signal regions, and 7–66% for the less constrained single-bin regions. In both cases the largest uncertainties arise in the regions with the highest requirements on jet multiplicity (and in the single-bin case also on b-jet multiplicity or M_{J}^{Σ}) since in those cases the supporting measurements are more statistically limited and so provide less precise constraints on the background predictions.

In each of the three multi-bin signal regions the most important uncertainty is the closure systematic uncertainty associated with the multijet template method (3–6%), chiefly because of the dominance of this background component. In the single-bin signal regions the background normalisations are less constrained by the fit, and the statistical uncertainties associated with the multijet and $t\bar{t}$ control regions tend to dominate (4–27% for multijets, 6–14% for $t\bar{t}$).

The theoretical uncertainty on the $t\bar{t}$ background predictions is also found to be significant, with that from the final state radiation contributing up to 17% in the single-bin fits. The impact on the total yield in multi-bin signal regions is ≤5%. The Z+jets component has a theoretical uncertainty of up to 14% in the single-bin regions while it is at most ≤6% in the multi-bin signal regions.

Most experimental systematic uncertainties on the reconstructed objects have insignificant impacts, being substantially reduced due to correlations between the MC-based predictions and the data-driven multijet template. The largest observed effects are due to the uncertainties on the jet energy scale which can be up to 3%, due to the large jet activity in the events selected by this analysis, and on the soft term of the missing transverse momentum (≤10%). In the least populated SRs, there can be a large statistical uncertainty on the predictions from simulation.

Signal region	Total syst.	Dominant systematic uncertainties					
SR-8ij50-0ib-MJ500	16%	$E_{\mathrm{T}}^{\mathrm{miss}}$ soft, L	7%	$E_{\mathrm{T}}^{\mathrm{miss}}$ soft, T	7%	Z+jets PS	5%
SR-9ij50-0ib-MJ340	16%	$E_{\mathrm{T}}^{\mathrm{miss}}$ soft, T	9%	$E_{\mathrm{T}}^{\mathrm{miss}}$ soft, L	9%	Z+jets PS	4%
SR-10ij50-0ib-MJ340	20%	$t\bar{t}$ FSR	9%	MC stat.	9%	$E_{\mathrm{T}}^{\mathrm{miss}}$ soft, L	8%
SR-10ij50-0ib-MJ500	27%	$t\bar{t}$ FSR	17%	MC stat.	12%	$E_{\mathrm{T}}^{\mathrm{miss}}$ soft, L	9%
SR-10ij50-1ib-MJ500	24%	MC stat.	14%	$E_{\mathrm{T}}^{\mathrm{miss}}$ soft, L	10%	$E_{\mathrm{T}}^{\mathrm{miss}}$ soft, T	10%
SR-11ij50	27%	MC stat.	18%	$t\bar{t}$ FSR	14%	$t\bar{t}$ norm	6%
SR-12ij50-2ib	70%	MC stat.	62%	MJ norm	25%	MJ H_{T} binning	13%
SR-9ij80	21%	MC stat.	14%	Z+jets PS	14%	Z+jets match	7%
SR-8ij50 multi-bin	6%	MJ closure	3%	JES flavour	3%	JES flavour	2%
SR-9ij50 multi-bin	7%	MJ closure	4%	Z+jets PS	3%	$E_{\mathrm{T}}^{\mathrm{miss}}$ soft, L	3%
SR-10ij50 multi-bin	14%	Z+jets PS	6%	MJ closure	6%	$t\bar{t}$ FSR	5%

Table 9: The total systematic uncertainties are shown for each of the single-bin signal regions, and also for the multi-bin signal regions, together with the three dominant contributions for each. The individual uncertainties can be (anti-)correlated, and do not necessarily sum quadratically to the total background uncertainty. For the multi-bin signal regions the uncertainties are those found after summing the expected yields over the corresponding M_{J}^{Σ} and b-jet multiplicity bins of Table 2. Within the table 'MC stat.' indicates the statistical uncertainty on simulated events in the SR, 'MJ' indicates the uncertainty on the multijet background, 'closure' indicates the uncertainty from the multijet template method closure, 'norm' is the result of statistical uncertainties from the CRs, 'JES flavour' indicates the uncertainties on the jet energy scale due to differences between quark- and gluon-initiated jets, '$E_{\mathrm{T}}^{\mathrm{miss}}$ soft, L/T' indicate two sources, longitudinal and transverse, of uncertainty on the soft component of the missing transverse momentum, 'MJ H_{T} binning' relates to the parameters of the binning of the multijet template in H_{T}, 'FSR' indicates final state radiation, 'match' indicates the matrix element/parton shower matching scale, and 'PS' is the uncertainty from varying the scale at which the strong coupling constant is calculated for parton shower emissions in the MC calculation.

7 Results and interpretation

Data yields are shown graphically for all signal regions in Figure 8. The background predicted to have the largest yield in all signal regions is multijet production. The relative contribution of the remaining backgrounds depends on the signal region. The $t\bar{t}$ process generally provides the second-largest contribution, and tends to form a larger fraction of the total background for larger jet multiplicity requirements. As the requirement on the number of b-tagged jets increases it can be seen that the relative contributions of W+jets, Z+jets and multi-boson backgrounds decrease compared to those from $t\bar{t}$ and single-top-quark production processes.

A breakdown of the yields in the single-bin regions is given in Table 10. For illustration, the full $\mathcal{S}(E_{\mathrm{T}}^{\mathrm{miss}})$ distributions for several signal regions are shown in Figure 9. The data yields are found to be consistent with the background predictions within the assessed statistical and systematic uncertainties, with no significant excesses over the SM expectation. Mild deviations are observed, with a tendency for the background to be overestimated in the higher jet multiplicity regions, which is consistent with the trends observed in the corresponding validation regions. For interpretation, the likelihood fits for background estimation (Section 6.3) are extended to include the signal region, and thereby perform two forms of hypothesis test using a profile-likelihood-ratio test statistic [85], quantifying the significance of any observed excesses or the lack thereof.

Firstly, the discovery test discriminates between the null hypothesis stating that the SR measurement is consistent with only SM contributions and an alternative hypothesis postulating a positive signal. Secondly, assuming a specific signal model, one may also form an exclusion test of the signal-plus-background hypothesis, where an observation significantly smaller than the combination of SM and SUSY processes would lead to rejection of the signal model. This provides the exclusion p-value p_1, the probability of observing at most the observed event yield under the assumption that the signal is present with its nominal cross-section. A complementary p-value for the background observation $\mathrm{CL_b}$ is defined as the probability of observing at most the observed yield under the background-only hypothesis. Points in the SUSY parameter space are considered excluded if the $\mathrm{CL_s}$ parameter [86], computed as $p_1/(1-\mathrm{CL_b})$ is smaller than 0.05. This protects against spurious exclusion of signals due to observing SR event counts significantly smaller than those predicted. While not strictly defining a frequentist confidence level, these are referred to as 95% confidence level (CL) limits.

The single-bin signal region event yields are used to derive model-independent constraints on the production of BSM particles. Table 11 shows the observed 95% CL limits on the visible cross-section $\langle\epsilon\sigma\rangle_{\mathrm{obs}}^{95}$ as well as the observed (expected) limits on the number of BSM signal events S_{obs}^{95} (S_{exp}^{95}) in each signal region. The discovery p-value $p(s=0)$, defined as probability of observing at least the observed event yield under the assumption that no signal is present, is calculated, as is the corresponding gaussian significance Z. For signal regions in which the predictions exceed the data, the value of $p(s=0)$ is capped at 0.5. The smallest background p-value $\mathrm{CL_b}$ computed in any region is 16%, while the smallest discovery p-value is 0.41, hence all observations are compatible with the SM-only hypothesis. The most stringent limits observed are for the `SR-12ij50-2ib` selection, for which visible cross-sections greater than 40 ab are excluded.

Constraints on sparticle production in several benchmark parameter planes are shown in Figure 10. These limits extend beyond those achieved by the previous search [16]. All exclusion fits are consistent with the background-only hypothesis, considering the total uncertainties.

For all three signal scenarios, the multi-bin limits provide the strongest expected constraints. There are two exceptions: the `SR-9ij80-0ib` selection reaches parity with the multi-bin limits for small neutralino masses

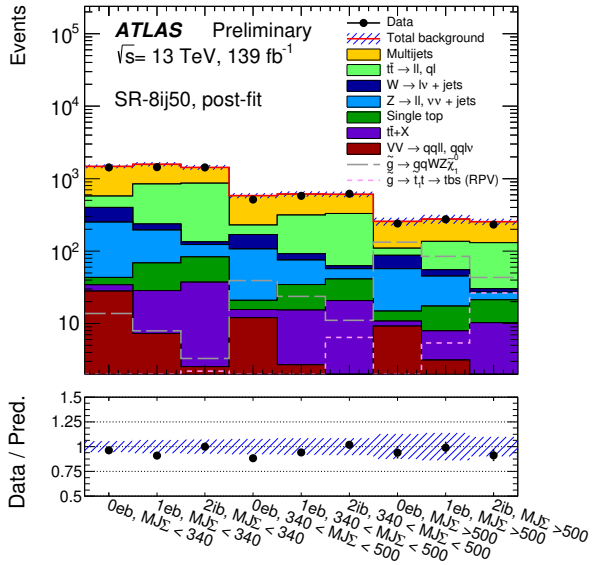

(a) SR-8ij50, multi-bin

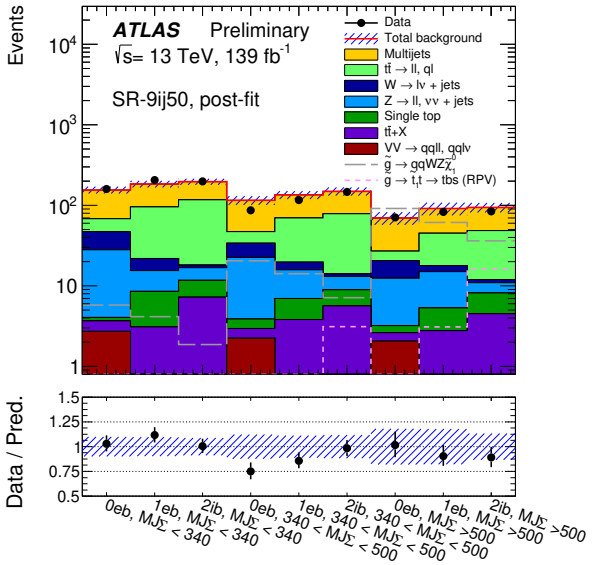

(b) SR-9ij50, multi-bin

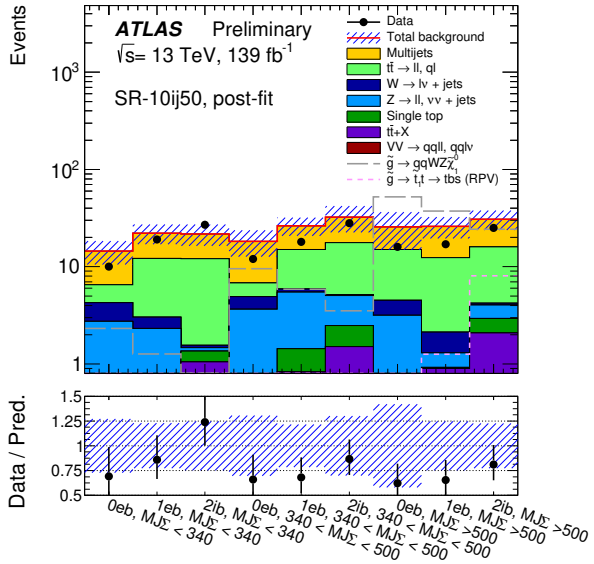

(c) SR-10ij50, multi-bin

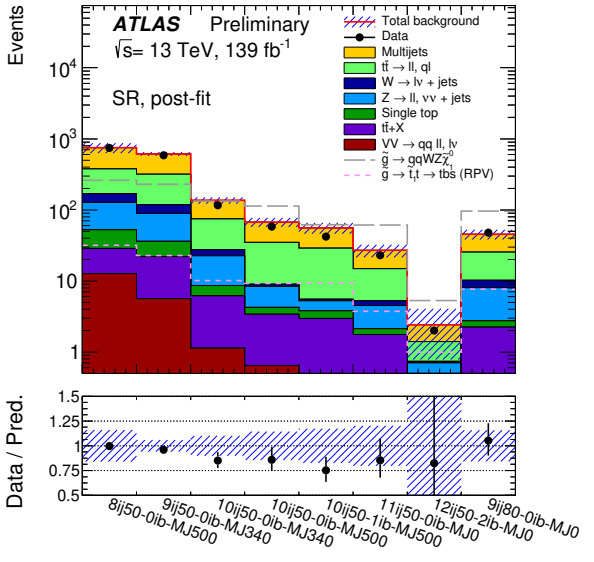

(d) Single-bin summary

Figure 8: Event yields in all signal regions, comparing data with the post-fit background predictions. The upper panel shows the absolute yields for data (black points) and all background subcomponents (histograms), with the combination of statistical and systematic uncertainties shown by the hatched areas. The yields for two benchmark signal models are overlaid, representing 1.6 TeV gluinos decaying to W and Z bosons and a 100 GeV neutralino via intermediate gauginos (long dashed histogram) or instead to tbs/tbd via a 600 GeV top squark through an R-parity violating (RPV) coupling (short dashed histogram). The lower panel shows the ratio of the data yields to the total SM prediction.

Background process	SR-8ij50-0ib-MJ500	SR-9ij50-0ib-MJ340
Multijets	372 ± 46	296 ± 39
Top quark pairs	208 ± 89	201 ± 65
W+jets	41 ± 20	29 ± 12
Z+jets	75 ± 46	53 ± 33
Single top quarks	23.9 ± 10.5	14.1 ± 5.3
$t\bar{t} + X$	16.1 ± 8.3	16.4 ± 8.4
Diboson, triboson	12.7 ± 1.7	5.6 ± 1.3
Total background	750 ± 120	614 ± 97
Observed events	747	588

Background process	SR-10ij50-0ib-MJ340	SR-10ij50-0ib-MJ500	SR-10ij50-1ib-MJ500
Multijets	62 ± 11	32.8 ± 6.1	26.9 ± 6.8
Top quark pairs	47 ± 17	26 ± 15	23.5 ± 9.8
W+jets	4.9 ± 2.7	$0.6^{+1.0}_{-0.6}$	$0.3^{+0.4}_{-0.3}$
Z+jets	14 ± 13	4 ± 4	$1.5^{+1.6}_{-1.5}$
Single top quarks	2.4 ± 1.7	$0.9^{+1.7}_{-0.9}$	$0.8^{+1.1}_{-0.8}$
$t\bar{t} + X$	5.0 ± 2.6	2.7 ± 1.5	2.7 ± 1.5
Diboson, triboson	1.13 ± 0.24	0.65 ± 0.19	0.26 ± 0.06
Total background	136 ± 28	68 ± 18	56 ± 13
Observed events	116	58	42

Background process	SR-11ij50	SR-12ij50-2ib	SR-9ij80
Multijets	12.0 ± 3.8	1.03 ± 0.99	20.0 ± 5.1
Top quark pairs	9.7 ± 4.5	0.66 ± 0.53	15.3 ± 4.0
W+jets	0.75 ± 0.75	$0.04^{+0.08}_{-0.04}$	2.2 ± 1.2
Z+jets	2.4 ± 1.4	0.50 ± 0.31	$5.3^{+5.4}_{-5.3}$
Single top quarks	$0.4^{+1.6}_{-0.4}$	0.00 ± 0.00	$0.50^{+0.71}_{-0.50}$
$t\bar{t} + X$	1.4 ± 0.8	0.20 ± 0.19	1.9 ± 1.0
Diboson, triboson	0.31 ± 0.06	0.00 ± 0.00	0.32 ± 0.06
Total background	27.0 ± 7.3	2.4 ± 1.7	45.6 ± 9.5
Observed events	23	2	48

Table 10: Detailed event yields in all single-bin signal regions. Due to correlations, summing the uncertainties on individual background components may not reproduce the final uncertainty on the total background prediction.

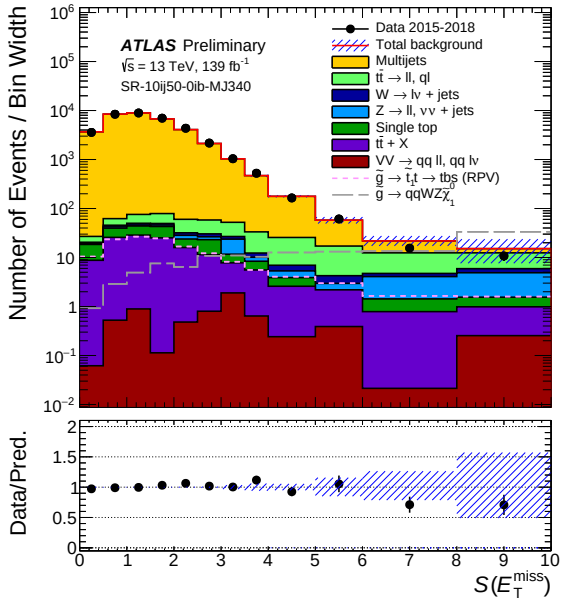

(a) SR-10ij50-0ib-MJ340

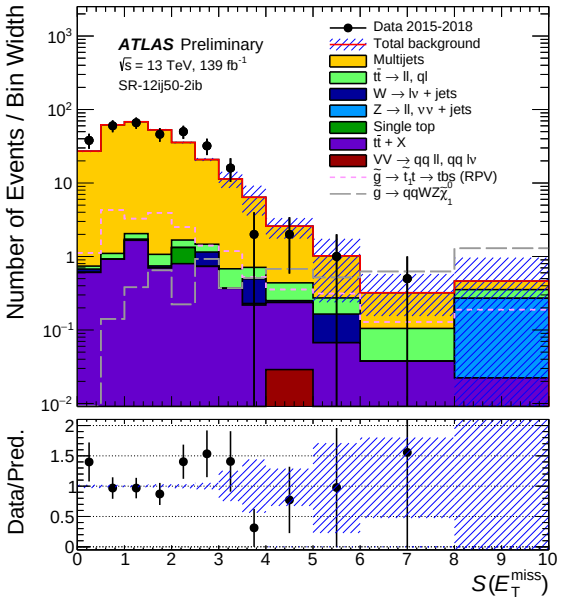

(b) SR-12ij50-2ib

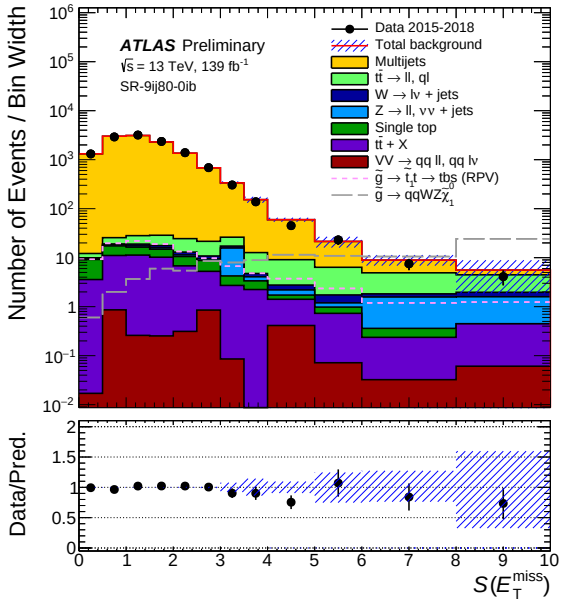

(c) SR-9ij80

Figure 9: Distribution of $\mathcal{S}(E_{\mathrm{T}}^{\mathrm{miss}})$ in selected signal regions. The $t\bar{t}$ and W+jets backgrounds have been normalised according to the background fits, and the multijet background subtraction adjusted accordingly. The upper panel shows the absolute yields for data (black points) and all background subcomponents (histograms), with the combination of statistical and systematic uncertainties shown by the hatched areas. The yields for two benchmark signal models are overlaid, representing 1.6 TeV gluinos decaying to W and Z bosons and a 100 GeV neutralino via intermediate gauginos (long dashed histogram) or instead to tbs/tbd via a 600 GeV top squark through an R-parity violating (RPV) coupling (short dashed histogram). The lower panel shows the ratio of the data yields to the total SM prediction.

Signal channel	$\langle\epsilon\sigma\rangle^{95}_{\text{obs}}$ [fb]	S^{95}_{obs}	S^{95}_{exp}	CL_b	$p(s=0)$ (Z)
SR-8ij50-0ib-MJ500	1.16	163	162^{+33}_{-39}	0.50	0.50 (0.00)
SR-9ij50-0ib-MJ340	0.95	133	140^{+30}_{-31}	0.50	0.50 (0.00)
SR-10ij50-0ib-MJ340	0.22	31	40^{+15}_{-11}	0.21	0.50 (0.00)
SR-10ij50-0ib-MJ500	0.16	21.9	$25.9^{+9.6}_{-6.8}$	0.29	0.50 (0.00)
SR-10ij50-1ib-MJ500	0.12	16.8	$22.8^{+8.5}_{-6.1}$	0.16	0.50 (0.00)
SR-11ij50	0.09	13.0	$15.1^{+6.0}_{-4.2}$	0.32	0.50 (0.00)
SR-12ij50-2ib	0.04	5.0	$5.2^{+2.5}_{-1.7}$	0.44	0.50 (0.00)
SR-9ij80	0.18	25.2	$24.5^{+7.0}_{-6.3}$	0.57	0.41 (0.22)

Table 11: Left to right: 95% CL upper limits on the visible cross-section ($\langle\epsilon\sigma\rangle^{95}_{\text{obs}}$) and on the number of signal events (S^{95}_{obs}). The third column (S^{95}_{exp}) shows the 95% CL upper limit on the number of signal events, given the expected number (and $\pm1\sigma$ excursions around the expectation) of background events. The last two columns indicate the CL_b value, i.e. the confidence level observed for the background-only hypothesis, and the discovery p-value ($p(s=0)$), together with the corresponding Gaussian significance (Z).

in the two-step gluino decay model, while at low gluino mass in the RPV decay the SR-8ij50-0ib-MJ500 single-bin region achieves better sensitivity for small mass-splittings, but only for signal models already excluded by previous searches. More significantly, the multi-bin approach enhances the sensitivity to RPV decays of the gluino, as well as to gluino-mediated stop production in the region where the LSP is moderately massive. The 8-jet multi-bin region is most sensitive where the gluino-neutralino mass-splitting is smaller, while the 9- and 10-jet selections take over as the mass-splitting increases, which allows for better signal-background discrimination with a harsher selection.

The tightest bounds on the gluino mass are placed at $m_{\tilde{g}} > 2$ TeV for gluinos decaying via a two-step cascade to W and Z bosons under the assumption of massless neutralinos. For gluino decays to a $t\bar{t}$ pair and $E_{\text{T}}^{\text{miss}}$ via RPC couplings, the region with $m_{\tilde{g}} < 1.8$ TeV and $m_{\tilde{\chi}^0_1} < 700$ GeV is excluded, with the highest excluded neutralino mass being $m_{\tilde{\chi}^0_1} \simeq 950$ GeV. This represents an improvement of 260 GeV in $m_{\tilde{g}}$ and 230 GeV in $m_{\tilde{\chi}^0_1}$ with respect to the previous search results. In the case of stop-mediated gluino decays via RPV couplings, the reach in $m_{\tilde{g}}$ is above 1.5 TeV for $\tilde{t}_1$ masses of 400 GeV to 1.1 TeV, with the maximal reach being achieved at 1.6 TeV for $m_{\tilde{t}_1} = 900$ GeV.

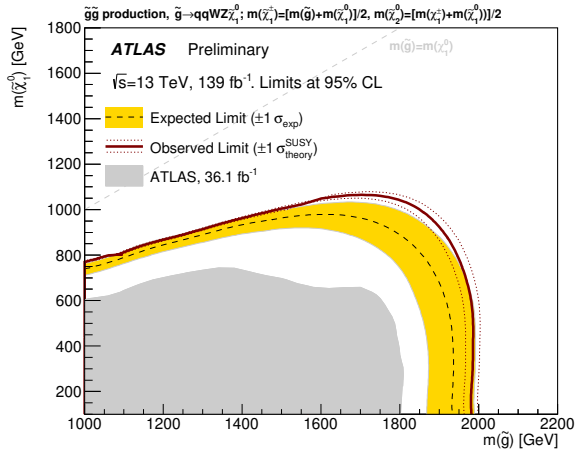

(a) $\tilde{g}$, 2-step cascade

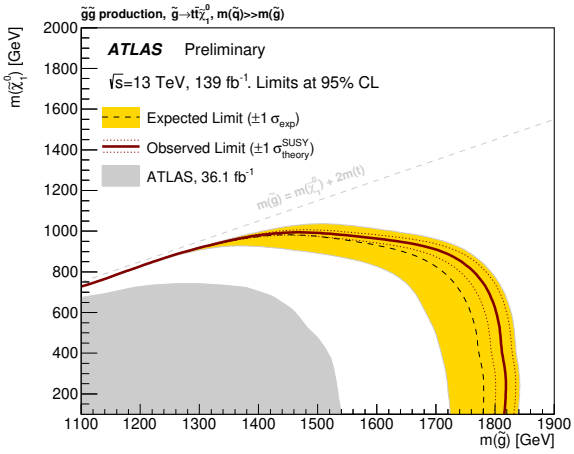

(b) $\tilde{g} \rightarrow t\bar{t}\tilde{\chi}_1^0$

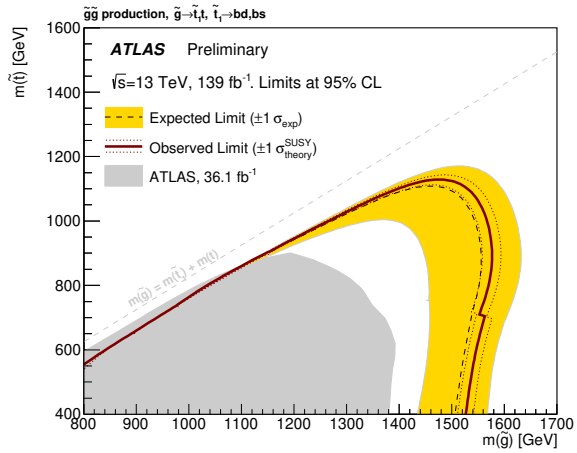

(c) RPV $\tilde{g} \rightarrow tbd, tbs$

Figure 10: Exclusion limits on gluino production in various parameter planes. The solid maroon line indicates the observed exclusion limit at 95% CL. Transitions between two signal regions which provide the best expected sensitivity in different regions of the parameter space may lead to discontinuities in the observed limit. A dashed black line and yellow band respectively indicate the expected limit and its 1σ variations due to all uncertainties on the signal acceptance and background yields. Grey shading is used to indicate the observed limit from the previous publication [16].

8 Conclusion

A search for new physics, producing many jets and moderate $E_{\mathrm{T}}^{\mathrm{miss}}$, is presented, using the pp dataset collected by ATLAS during Run 2 of the LHC. The analysis selects events in regions with large jet multiplicities (from ≥8 to ≥12 jets) with further requirements on the number of b-tagged jets, and on the sum of the masses of large-radius jets. This search is the first from ATLAS to exploit particle-flow reconstruction for jets and $E_{\mathrm{T}}^{\mathrm{miss}}$. The combination of this improvement together with a better object-based $\mathcal{S}(E_{\mathrm{T}}^{\mathrm{miss}})$ definition and a multi-bin statistical analysis leads to significant improvements in the search sensitivity beyond that afforded simply by the larger dataset.

No significant deviations from the Standard Model expectations are observed, while limits on the production of new particles are significantly extended. In the context of R-parity conserving supersymmetry, limits on the gluino mass reach 2 TeV in the case of a two-step cascade via vector bosons, which are the most stringent for a low-mass $\tilde{\chi}_1^0$. For gluino-pair production followed by the decay $\tilde{g} \to t\bar{t}\tilde{\chi}_1^0$ gluino masses up to 1.8 TeV are excluded for $\tilde{\chi}_1^0$ masses up to 700 GeV. In the case of gluino-pair production followed by the R-parity violating decays, $\tilde{g} \to tbd, tbs$, limits extend up to 1.6 TeV for a $\tilde{t}$ mass of 900 GeV. Model-independent upper limits on the visible cross-section are set as low as 40 ab, in signal regions that probe extremely large jet multiplicities, with the most stringent selections requiring ≥12 jets of which two are b-tagged.

References

[1] L. Evans and P. Bryant, *LHC Machine*, JINST **3** (2008) S08001.

[2] Y. A. Golfand and E. Likhtman, *Extension of the Algebra of Poincare Group Generators and Violation of p Invariance*, JETP Lett. **13** (1971) 323, [Pisma Zh. Eksp. Teor. Fiz. **13** (1971) 452].

[3] D. V. Volkov and V. P. Akulov, *Is the neutrino a goldstone particle?*, Phys. Lett. B **46** (1973) 109.

[4] J. Wess and B. Zumino, *Supergauge transformations in four dimensions*, Nucl. Phys. B **70** (1974) 39.

[5] J. Wess and B. Zumino, *Supergauge invariant extension of quantum electrodynamics*, Nucl. Phys. B **78** (1974) 1.

[6] S. Ferrara and B. Zumino, *Supergauge invariant Yang-Mills theories*, Nucl. Phys. B **79** (1974) 413.

[7] A. Salam and J. A. Strathdee, *Super-symmetry and non-Abelian gauges*, Phys. Lett. B **51** (1974) 353.

[8] G. R. Farrar and P. Fayet, *Phenomenology of the production, decay, and detection of new hadronic states associated with supersymmetry*, Phys. Lett. B **76** (1978) 575.

[9] H. Dreiner, *An introduction to explicit R-parity violation*, Pramana **51** (1998) 123.

[10] ATLAS Collaboration, *The ATLAS Experiment at the CERN Large Hadron Collider*, JINST **3** (2008) S08003.

[11] T. Cohen, E. Izaguirre, M. Lisanti and H. K. Lou, *Jet substructure by accident*, JHEP **03** (2013) 161, arXiv: 1212.1456 [hep-ph].

[12] ATLAS Collaboration, *Search for new phenomena in final states with large jet multiplicities and missing transverse momentum using $\sqrt{s}$ = 7 TeV pp collisions with the ATLAS detector*, JHEP **11** (2011) 099, arXiv: 1110.2299 [hep-ex].

[13] ATLAS Collaboration, *Hunt for new phenomena using large jet multiplicities and missing transverse momentum with ATLAS in* $4.7\,fb^{-1}$ *of* $\sqrt{s} = 7$ *TeV proton–proton collisions*, JHEP **07** (2012) 167, arXiv: 1206.1760 [hep-ex].

[14] ATLAS Collaboration, *Search for new phenomena in final states with large jet multiplicities and missing transverse momentum at* $\sqrt{s} = 8$ *TeV proton-proton collisions using the ATLAS experiment*, JHEP **10** (2013) 130, arXiv: 1308.1841 [hep-ex], Erratum: JHEP **01** (2014) 109.

[15] ATLAS Collaboration, *Search for new phenomena in final states with large jet multiplicities and missing transverse momentum with ATLAS using* $\sqrt{s} = 13$ *TeV proton–proton collisions*, Phys. Lett. B **757** (2016) 334, arXiv: 1602.06194 [hep-ex].

[16] ATLAS Collaboration, *Search for new phenomena with large jet multiplicities and missing transverse momentum using large-radius jets and flavour-tagging at ATLAS in* 13 *TeV pp collisions*, JHEP **12** (2017) 034, arXiv: 1708.02794 [hep-ex].

[17] ATLAS Collaboration, *Jet reconstruction and performance using particle flow with the ATLAS Detector*, Eur. Phys. J. C **77** (2017) 466, arXiv: 1703.10485 [hep-ex].

[18] ATLAS Collaboration, *Object-based missing transverse momentum significance in the ATLAS Detector*, ATLAS-CONF-2018-038, 2018, URL: https://cds.cern.ch/record/2630948.

[19] ATLAS Collaboration, *ATLAS Insertable B-Layer Technical Design Report*, ATLAS-TDR-19, 2010, URL: https://cds.cern.ch/record/1291633, Addendum: ATLAS-TDR-19-ADD-1, 2012, URL: https://cds.cern.ch/record/1451888.

[20] B. Abbott et al., *Production and integration of the ATLAS Insertable B-Layer*, JINST **13** (2018) T05008, arXiv: 1803.00844 [physics.ins-det].

[21] ATLAS Collaboration, *Performance of the ATLAS trigger system in 2015*, Eur. Phys. J. C **77** (2017) 317, arXiv: 1611.09661 [hep-ex].

[22] ATLAS Collaboration, *Luminosity determination in pp collisions at* $\sqrt{s} = 13$ *TeV using the ATLAS detector at the LHC*, ATLAS-CONF-2019-021, 2019, URL: https://cds.cern.ch/record/2677054.

[23] G. Avoni et al., *The new LUCID-2 detector for luminosity measurement and monitoring in ATLAS*, JINST **13** (2018) P07017.

[24] ATLAS Collaboration, *Trigger Menu in 2017*, ATL-DAQ-PUB-2018-002, 2018, URL: https://cds.cern.ch/record/2625986.

[25] ATLAS Collaboration, *ATLAS data quality operations and performance for 2015-2018 data-taking*, (2019), arXiv: 1911.04632 [physics.ins-det].

[26] ATLAS Collaboration, *Characterisation and mitigation of beam-induced backgrounds observed in the ATLAS detector during the 2011 proton-proton run*, JINST **8** (2013) P07004, arXiv: 1303.0223 [hep-ex].

[27] ATLAS Collaboration, *Selection of jets produced in* 13 *TeV proton–proton collisions with the ATLAS detector*, ATLAS-CONF-2015-029, 2015, URL: https://cds.cern.ch/record/2037702.

[28] T. Sjöstrand, S. Mrenna and P. Z. Skands, *A brief introduction to PYTHIA 8.1*, Comput. Phys. Commun. **178** (2008) 852, arXiv: 0710.3820 [hep-ph].

[29] ATLAS Collaboration, *The Pythia 8 A3 tune description of ATLAS minimum bias and inelastic measurements incorporating the Donnachie–Landshoff diffractive model*, ATL-PHYS-PUB-2016-017, 2016, URL: https://cds.cern.ch/record/2206965.

[30] R. D. Ball et al., *Parton distributions with LHC data*, Nucl. Phys. B **867** (2013) 244, arXiv: 1207.1303 [hep-ph].

[31] ATLAS Collaboration, *The ATLAS Simulation Infrastructure*, Eur. Phys. J. C **70** (2010) 823, arXiv: 1005.4568 [physics.ins-det].

[32] S. Agostinelli et al., *GEANT4 – a simulation toolkit*, Nucl. Instrum. Meth. A **506** (2003) 250.

[33] ATLAS Collaboration, *Performance of the Fast ATLAS Tracking Simulation (FATRAS) and the ATLAS Fast Calorimeter Simulation (FastCaloSim) with single particles*, ATL-SOFT-PUB-2014-01, 2014, URL: https://cds.cern.ch/record/1669341.

[34] P. Nason, *A new method for combining NLO QCD with shower Monte Carlo algorithms*, JHEP **11** (2004) 040, arXiv: hep-ph/0409146.

[35] S. Frixione, P. Nason and C. Oleari, *Matching NLO QCD computations with parton shower simulations: the POWHEG method*, JHEP **11** (2007) 070, arXiv: 0709.2092 [hep-ph].

[36] S. Alioli, P. Nason, C. Oleari and E. Re, *A general framework for implementing NLO calculations in shower Monte Carlo programs: the POWHEG BOX*, JHEP **06** (2010) 043, arXiv: 1002.2581 [hep-ph].

[37] S. Alioli, P. Nason, C. Oleari and E. Re, *NLO single-top production matched with shower in POWHEG: s- and t-channel contributions*, JHEP **09** (2009) 111, arXiv: 0907.4076 [hep-ph], Erratum: JHEP **02** (2010) 011.

[38] E. Re, *Single-top Wt-channel production matched with parton showers using the POWHEG method*, Eur. Phys. J. C **71** (2011), arXiv: 1009.2450 [hep-ph].

[39] S. Alioli, S.-O. Moch and P. Uwer, *Hadronic top-quark pair-production with one jet and parton showering*, JHEP **01** (2012) 137, arXiv: 1110.5251 [hep-ph].

[40] R. D. Ball et al., *Parton distributions for the LHC Run II*, JHEP **04** (2015) 040, arXiv: 1410.8849 [hep-ph].

[41] S. Frixione, E. Laenen, P. Motylinski, B. R. Webber and C. D. White, *Single-top hadroproduction in association with a W boson*, JHEP **07** (2008) 029, arXiv: 0805.3067 [hep-ph].

[42] P. Artoisenet, R. Frederix, O. Mattelaer and R. Rietkerk, *Automatic spin-entangled decays of heavy resonances in Monte Carlo simulations*, JHEP **03** (2013) 015, arXiv: 1212.3460 [hep-ph].

[43] T. Sjöstrand et al., *An introduction to PYTHIA 8.2*, Comput. Phys. Commun. **191** (2015) 159, arXiv: 1410.3012 [hep-ph].

[44] ATLAS Collaboration, *ATLAS Pythia 8 tunes to 7 TeV data*, ATL-PHYS-PUB-2014-021, 2014, URL: https://cds.cern.ch/record/1966419.

[45] D. J. Lange, *The EvtGen particle decay simulation package*, Nucl. Instrum. Meth. A **462** (2001) 152.

[46] T. Gleisberg et al., *Event generation with SHERPA 1.1*, JHEP **02** (2009) 007, arXiv: 0811.4622 [hep-ph].

[47] M. Czakon and A. Mitov, *Top++: A program for the calculation of the top-pair cross-section at hadron colliders*, Comput. Phys. Commun. **185** (2014) 2930, arXiv: 1112.5675 [hep-ph].

[48] N. Kidonakis, *Two-loop soft anomalous dimensions for single top quark associated production with a W- or H-*, Phys. Rev. D **82** (2010) 054018, arXiv: 1005.4451 [hep-ph].

[49] N. Kidonakis, '*Top Quark Production*', *Proceedings, Helmholtz International Summer School on Physics of Heavy Quarks and Hadrons (HQ 2013)*, 2014 139, arXiv: 1311.0283 [hep-ph].

[50] M. Aliev et al., *HATHOR: HAdronic Top and Heavy quarks crOss section calculatoR*, Comput. Phys. Commun. **182** (2011) 1034, arXiv: 1007.1327 [hep-ph].

[51] P. Kant et al., *HatHor for single top-quark production: Updated predictions and uncertainty estimates for single top-quark production in hadronic collisions*, Comput. Phys. Commun. **191** (2015) 74, arXiv: 1406.4403 [hep-ph].

[52] J. Alwall et al., *The automated computation of tree-level and next-to-leading order differential cross sections, and their matching to parton shower simulations*, JHEP **07** (2014) 079, arXiv: 1405.0301 [hep-ph].

[53] T. Gleisberg and S. Höche, *Comix, a new matrix element generator*, JHEP **12** (2008) 039, arXiv: 0808.3674 [hep-ph].

[54] F. Cascioli, P. Maierhöfer and S. Pozzorini, *Scattering Amplitudes with Open Loops*, Phys. Rev. Lett. **108** (2012) 111601, arXiv: 1111.5206 [hep-ph].

[55] S. Schumann and F. Krauss, *A parton shower algorithm based on Catani-Seymour dipole factorisation*, JHEP **03** (2008) 038, arXiv: 0709.1027 [hep-ph].

[56] S. Höche, F. Krauss, S. Schumann and F. Siegert, *QCD matrix elements and truncated showers*, JHEP **05** (2009) 053, arXiv: 0903.1219 [hep-ph].

[57] ATLAS Collaboration, *Improvements in $t\bar{t}$ modelling using NLO+PS Monte Carlo generators for Run 2*, ATL-PHYS-PUB-2018-009, 2018, URL: https://cds.cern.ch/record/2630327.

[58] M. Bähr et al., *Herwig++ physics and manual*, Eur. Phys. J. C **58** (2008) 639, arXiv: 0803.0883 [hep-ph].

[59] J. Bellm et al., *Herwig 7.0/Herwig++ 3.0 release note*, Eur. Phys. J. C **76** (2016) 196, arXiv: 1512.01178 [hep-ph].

[60] L. A. Harland-Lang, A. D. Martin, P. Motylinski and R. S. Thorne, *Parton distributions in the LHC era: MMHT 2014 PDFs*, Eur. Phys. J. C **75** (2015), arXiv: 1412.3989 [hep-ph].

[61] ATLAS Collaboration, *Multi-Boson Simulation for* 13 *TeV ATLAS Analyses*, ATL-PHYS-PUB-2017-005, 2017, URL: https://cds.cern.ch/record/2261933.

[62] ATLAS Collaboration, *ATLAS simulation of boson plus jets processes in Run 2*, ATL-PHYS-PUB-2017-006, 2017, URL: https://cds.cern.ch/record/2261937.

[63] L. Lönnblad, *Correcting the Colour-Dipole Cascade Model with Fixed Order Matrix Elements*, JHEP **2002** (2002) 046, arXiv: hep-ph/0112284.

[64] W. Beenakker, C. Borschensky, M. Krämer, A. Kulesza and E. Laenen, *NNLL-fast: predictions for coloured supersymmetric particle production at the LHC with threshold and Coulomb resummation*, JHEP **12** (2016) 133, arXiv: 1607.07741 [hep-ph].

[65] W. Beenakker et al., *NNLL resummation for squark and gluino production at the LHC*, JHEP **12** (2014) 023, arXiv: 1404.3134 [hep-ph].

[66] W. Beenakker et al., *Towards NNLL resummation: hard matching coefficients for squark and gluino hadroproduction*, JHEP **10** (2013) 120, arXiv: 1304.6354 [hep-ph].

[67] W. Beenakker et al., *NNLL resummation for squark-antisquark pair production at the LHC*, JHEP **01** (2012) 076, arXiv: 1110.2446 [hep-ph].

[68] W. Beenakker et al., *Soft-gluon resummation for squark and gluino hadroproduction*, JHEP **12** (2009) 041, arXiv: 0909.4418 [hep-ph].

[69] A. Kulesza and L. Motyka, *Soft gluon resummation for the production of gluino-gluino and squark-antisquark pairs at the LHC*, Phys. Rev. D **80** (2009) 095004, arXiv: 0905.4749 [hep-ph].

[70] A. Kulesza and L. Motyka, *Threshold Resummation for Squark-Antisquark and Gluino-Pair Production at the LHC*, Phys. Rev. Lett. **102** (2009) 111802, arXiv: 0807.2405 [hep-ph].

[71] W. Beenakker, R. Höpker, M. Spira and P. Zerwas, *Squark and gluino production at hadron colliders*, Nucl. Phys. B **492** (1997) 51, arXiv: hep-ph/9610490.

[72] J. Butterworth et al., *PDF4LHC recommendations for LHC Run II*, J. Phys. G **43** (2016) 023001, arXiv: 1510.03865 [hep-ph].

[73] ATLAS Collaboration, *Vertex Reconstruction Performance of the ATLAS Detector at* $\sqrt{s} = 13$ *TeV*, ATL-PHYS-PUB-2015-026, 2015, URL: https://cds.cern.ch/record/2037717.

[74] ATLAS Collaboration, *Topological cell clustering in the ATLAS calorimeters and its performance in LHC Run 1*, Eur. Phys. J. C **77** (2017) 490, arXiv: 1603.02934 [hep-ex].

[75] ATLAS Collaboration, *Performance of pile-up mitigation techniques for jets in pp collisions at* $\sqrt{s} = 8$ *TeV using the ATLAS detector*, Eur. Phys. J. C **76** (2016) 581, arXiv: 1510.03823 [hep-ex].

[76] ATLAS Collaboration, *Jet reclustering and close-by effects in ATLAS Run 2*, ATLAS-CONF-2017-062, 2017, URL: https://cds.cern.ch/record/2275649.

[77] ATLAS Collaboration, *Optimisation of the ATLAS b-tagging performance for the 2016 LHC Run*, ATL-PHYS-PUB-2016-012, 2016, URL: https://cds.cern.ch/record/2160731.

[78] ATLAS Collaboration, *ATLAS b-jet identification performance and efficiency measurement with* $t\bar{t}$ *events in pp collisions at* $\sqrt{s} = 13$ *TeV*, (2019), arXiv: 1907.05120 [hep-ex].

[79] ATLAS Collaboration, *Electron and photon performance measurements with the ATLAS detector using the 2015–2017 LHC proton-proton collision data*, JINST **14** (2019) P12006, arXiv: 1908.00005 [hep-ex].

[80] ATLAS Collaboration, *Electron efficiency measurements with the ATLAS detector using 2012 LHC proton–proton collision data*, Eur. Phys. J. C **77** (2017) 195, arXiv: 1612.01456 [hep-ex].

[81] ATLAS Collaboration, *Muon reconstruction performance of the ATLAS detector in proton–proton collision data at* $\sqrt{s} = 13$ *TeV*, Eur. Phys. J. C **76** (2016) 292, arXiv: 1603.05598 [hep-ex].

[82] ATLAS Collaboration, *Muon reconstruction performance in early* $\sqrt{s} = 13$ *TeV data*, ATL-PHYS-PUB-2015-037, 2015, URL: https://cds.cern.ch/record/2047831.

[83] ATLAS Collaboration, *Performance of algorithms that reconstruct missing transverse momentum in* $\sqrt{s} = 8$ *TeV proton–proton collisions in the ATLAS detector*, Eur. Phys. J. C **77** (2017) 241, arXiv: 1609.09324 [hep-ex].

[84] M. Baak et al., *HistFitter software framework for statistical data analysis*, Eur. Phys. J. C **75** (2015) 153, arXiv: 1410.1280 [hep-ex].

[85] G. Cowan, K. Cranmer, E. Gross and O. Vitells, *Asymptotic formulae for likelihood-based tests of new physics*, Eur. Phys. J. C **71** (2011) 1554, arXiv: 1007.1727 [physics.data-an], Erratum: Eur. Phys. J. C **73** (2013) 2501.

[86] A. L. Read, *Presentation of search results: the* CL_S *technique*, J. Phys. G **28** (2002) 2693.

Appendix

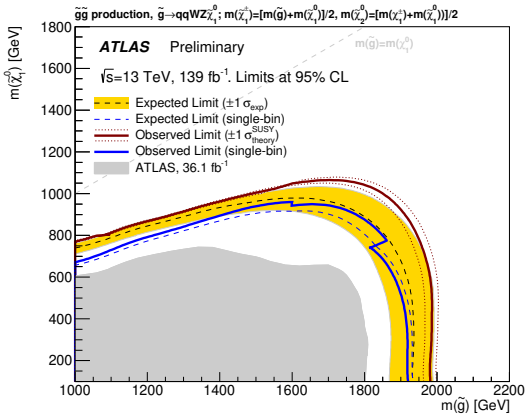

(a) $\tilde{g}$, 2-step cascade

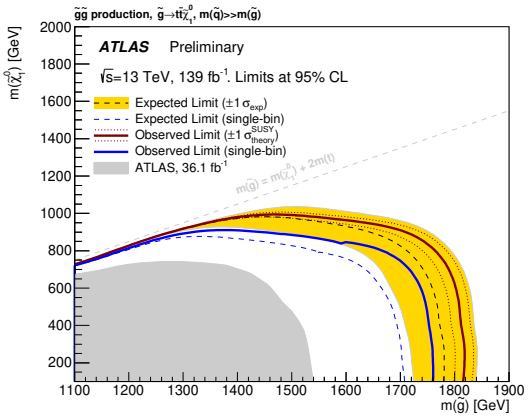

(b) $\tilde{g} \rightarrow t\bar{t}\tilde{\chi}_1^0$

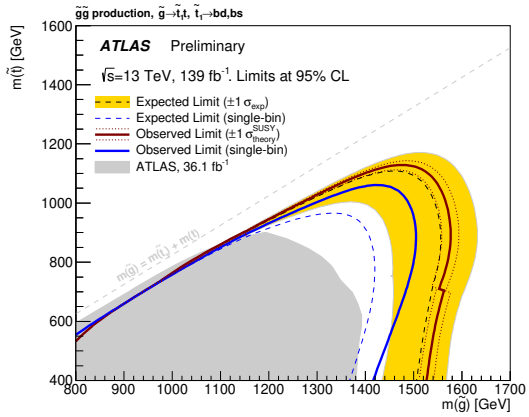

(c) RPV $\tilde{g} \rightarrow tbd, tbs$

Figure 11: Exclusion limits on gluino production in various parameter planes. The solid maroon line indicates the observed exclusion limit at 95% CL. A dashed black line and yellow band respectively indicate the expected limit and its 1σ variations due to all uncertainties on the signal acceptance and background yields. For illustration, the dashed and solid blue lines show the expected and observed limits considering the single-bin selections only. Grey shading is used to demarcate the observed limit from the previous publication [16].

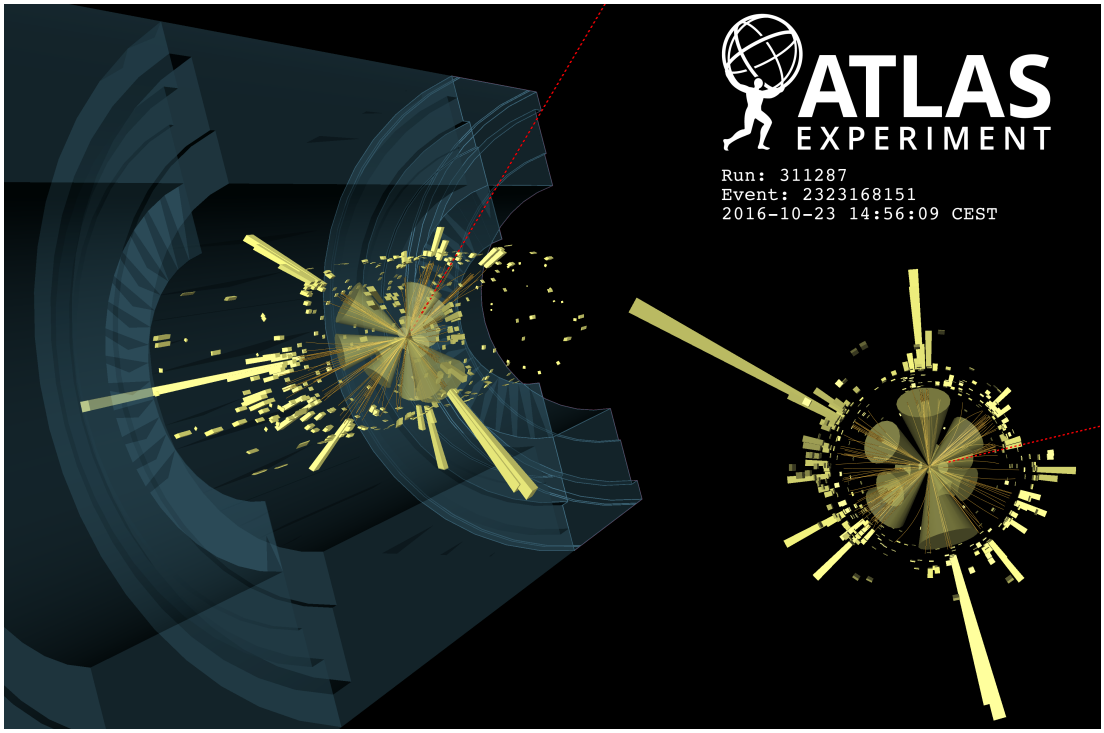

Figure 12: Visualisation of the highest jet multiplicity event selected in signal regions targeting long cascade decays of pair-produced gluinos. This event was recorded by ATLAS on 23 October 2016, and contains 16 jets, illustrated by cones. Yellow blocks represent the calorimeter energy measured in noise-suppressed clusters. Of the reconstructed jets, 13 (11) have transverse momenta above 50 GeV (80 GeV), with 3 (2) being b-tagged. The leading jet has a transverse momentum of 507 GeV, and the sum of jet transverse momenta H_T = 2.9 TeV. A value of 343 GeV is observed for the $E_{\mathrm{T}}^{\mathrm{miss}}$, whose direction is shown by the dashed red line, producing a significance $\mathcal{S}(E_{\mathrm{T}}^{\mathrm{miss}})$ = 6.4. The sum of the masses of large-radius jets is evaluated as M_{J}^{Σ} = 1070 GeV.

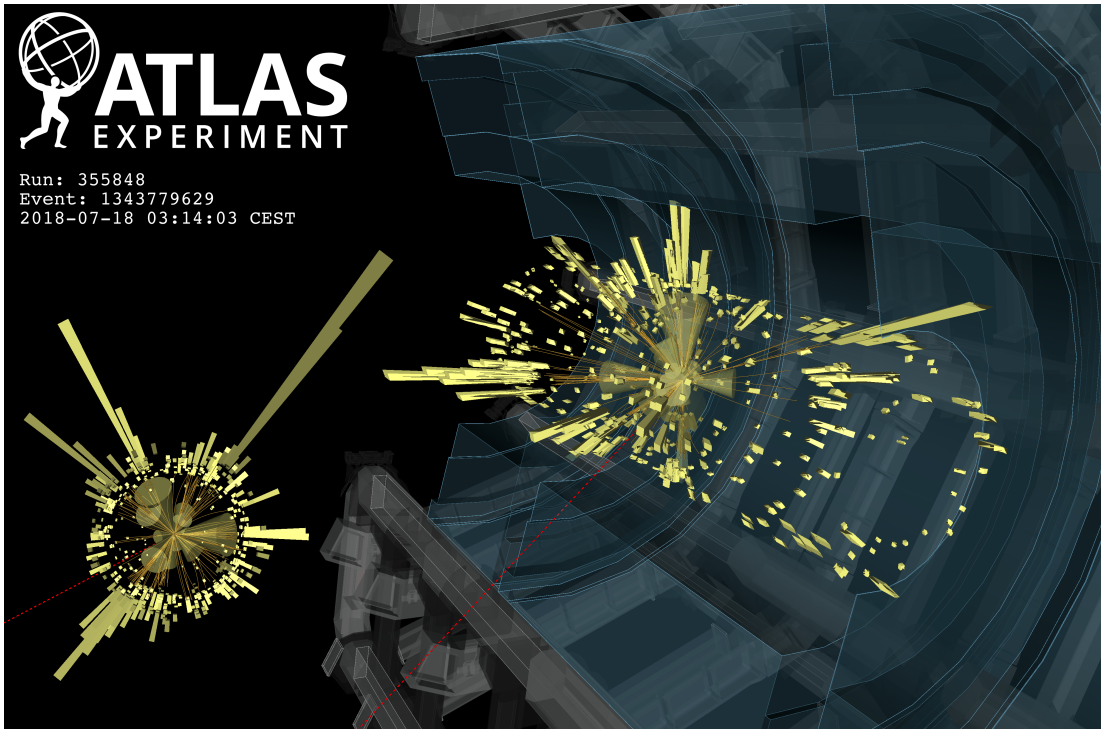

Figure 13: Visualisation of the highest jet multiplicity event selected in a control region used to make predictions of the background from multijet production. This event was recorded by ATLAS on 18 July 2018, and contains 19 jets, illustrated by cones. Yellow blocks represent the calorimeter energy measured in in noise-suppressed clusters. Of the reconstructed jets, 16 (10) have transverse momenta above 50 GeV (80 GeV). No jets are b-tagged. The leading jet has a transverse momentum of 371 GeV, and the sum of jet transverse momenta H_T = 2.2 TeV. A value of 8 GeV is observed for the $E_{\mathrm{T}}^{\mathrm{miss}}$, whose direction is shown by the dashed red line, producing a significance $\mathcal{S}(E_{\mathrm{T}}^{\mathrm{miss}}) = 0.2$. The sum of the masses of large-radius jets is evaluated as M_{J}^{Σ} = 767 GeV.

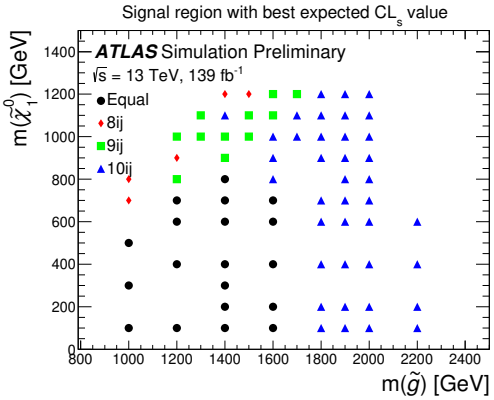

(a) $\tilde{g}$, 2-step cascade

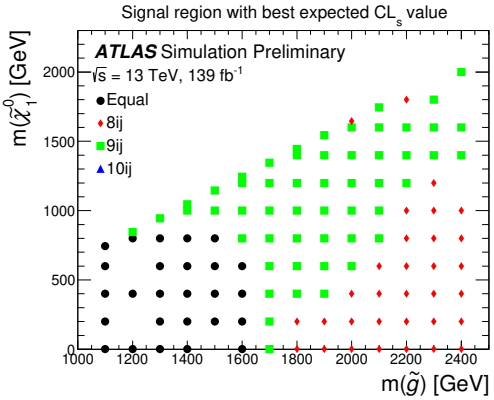

(b) $\tilde{g} \rightarrow t\bar{t}\tilde{\chi}_1^0$

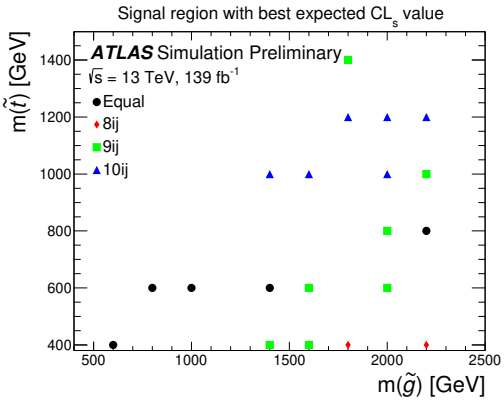

(c) RPV $\tilde{g} \rightarrow tbd, tbs$

Figure 14: The best expected signal regions corresponding to each mass point for gluino production in various parameter planes. These correspond to the jet multiplicity that yields the best expected CL_s value for a given signal mass point. The designation "Equal" means that two or more signal regions have the same best expected CL_s value.

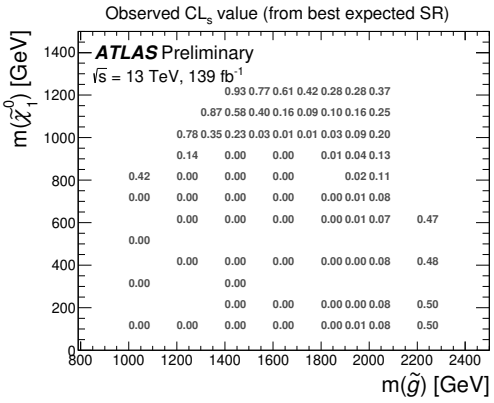

(a) $\tilde{g}$, 2-step cascade

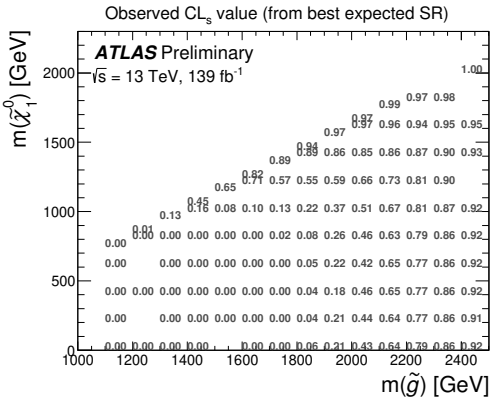

(b) $\tilde{g} \rightarrow t\bar{t}\tilde{\chi}_1^0$

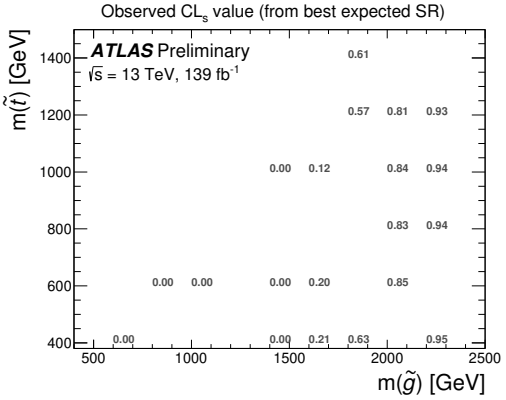

(c) RPV $\tilde{g} \rightarrow tbd, tbs$

Figure 15: The observed CL_s value corresponding to the best expected signal region in each mass point for gluino production in various parameter planes.